

Chapter 1

The Atomic-Scale Structure of Network Glass-Forming Materials

Philip S. Salmon and Anita Zeidler

Abstract A prerequisite for understanding the physico-chemical properties of network glass-forming materials is knowledge about their atomic-scale structure. The desired information is not, however, easy to obtain because structural disorder in a liquid or glass leads to complexity. It is therefore important to design experiments to give site-specific information on the structure of a given material in order to test the validity of different molecular dynamics models. In turn, once a molecular dynamics scheme contains the correct theoretical ingredients, it can be used both to enrich the information obtained from experiment and to predict the composition and temperature/pressure dependence of a material's properties, a first step in using the principles of rational design to prepare glasses with novel functional properties. In this chapter the symbiotic relationship between experiment and simulation is explored by focussing on the structures of liquid and glassy ZnCl_2 and GeSe_2 , and on the structure of glassy GeO_2 under pressure. Issues to be addressed include extended range ordering on a nanometre scale, the formation of homopolar (like-atom) bonds, and the density-driven mechanisms of network collapse.

1.1 Introduction

Network glass-forming materials are important in a broad range of scientific and technological disciplines, ranging from photonics [1] to magmas in planetary science [2]. It is therefore desirable to have realistic microscopic models of these materials in order to predict their behaviour when different chemical components are added, and when the state conditions are changed. A prerequisite for guiding in the development of a model is unambiguous information from experiment on the atomic-scale structure and dynamics in order to provide a critical test of its predictions.

P.S. Salmon (✉) · A. Zeidler
Department of Physics, University of Bath, Bath BA2 7AY, UK
e-mail: p.s.salmon@bath.ac.uk

A. Zeidler
e-mail: a.zeidler@bath.ac.uk

Structure refinement methods such as Reverse Monte Carlo (RMC) [3, 4] and Empirical Potential Structure Refinement (EPSR) [5, 6] are widely used by experimentalists to model measured diffraction data. In these methods, the atoms in a 3-dimensional starting model are moved in order to give configurations with diffraction patterns that are in agreement with experiment, subject to imposed constraints such as the measured number density, the inability of neighbouring particles to overlap, and the type and quantity of local structural units as provided by e.g. nuclear magnetic resonance (NMR) and/or extended x-ray absorption fine structure (EXAFS) spectroscopy experiments. The structural models therefore have the benefit of being consistent with the experimental data used in their construction¹ and, since they are based on 3-dimensional particle configurations, information can be obtained on three- and higher-body correlations. The reliability of the structural features in a given model will, however, depend on the sensitivity of the experimental data to the relevant correlations, the results for higher body correlations need to be treated with caution because diffraction data provides information only at the pair-correlation function level, and the final configurations can be sensitive to the choice of starting model as shown by work on SiO₂ glass [7, 8] and water [9–11]. For this reason, it is usually best to construct a realistic starting model so that the use of RMC or EPSR amounts to a refinement of that model using the experimental results as a reference.² Owing to the nature of their construction, RMC or EPSR models do not provide information on the particle dynamics, and since the modelling procedures are driven by experimental data they cannot be used if this information is unavailable i.e. the refinement methods have in this sense no predictive power.

Molecular dynamics methods, which are extensively used to model the structure of network glass-forming materials, also provide the atomic-scale dynamics (e.g. the vibrational density of states and self-diffusion coefficients), thus enriching the information made available on a given material. A comparison of this dynamical information with experiment can provide a particularly severe test for the validity of a model for a particular material. Furthermore, if the theory underlying the calculations has the correct ingredients then the simulations can be used to predict the composition and temperature/pressure dependence of a material's properties. Often-times, the search for the correct theoretical ingredients is not, however, trivial and different approaches involve trade-offs between e.g. the accuracy in describing a particular bonding scheme versus the number of atoms that can be dealt with on a realistic computational timescale.

For example, ionic interaction models can give an accurate description of the measured structure of glass-forming systems such as ZnCl₂ [14–17], provided that anion polarisation effects are taken into account [18–20], and the relative simplicity of these models allows for the coverage of relatively long length and time scales. Such models are, however, inappropriate for glass-forming materials such as GeSe₂ where

¹In the literature, the results from RMC or EPSR models are sometimes erroneously referred to as ‘experimental results’ when comparisons are made with molecular dynamics simulations.

²Increasingly, molecular dynamics is being used to provide the starting models for refinement procedures, see e.g. [12, 13].

the electronegativity difference between the atomic species is small and homopolar (like-atom) bonds are prevalent [21–23]. These features necessitate a first-principles density-functional based approach in which the electronic structure is taken into explicit account but where the simulation results can be sensitive to the choice of density functional [24–40]. These methods allow only for the investigation of relatively small systems for short times, although this may not be such an important issue when investigating e.g. the operation of phase-change memory alloys where the pertinent length and time scales are small relative to those associated with glass formation. In the investigation of glass-forming materials, there is also the question as how best to prepare accurate molecular dynamics models given the use of fast simulated quench-rates [37, 41–43].

In the following, the role of experiment in guiding molecular dynamics simulations of network glass-forming systems will be illustrated by considering a small set of materials with the MX_2 stoichiometry. Particular attention will be paid to the results obtained from the method of neutron diffraction with isotope substitution (NDIS) since it has been extensively used to obtain information at the partial structure factor level. An excellent starting point is provided by molten MX_2 salts where NDIS results have helped in the development of a reliable ionic interaction model for glass-forming materials like ZnCl_2 . Next, the GeSe_2 system is considered where NDIS results have played a major role in the continuing development of first-principles molecular dynamics methods for describing the structure and properties of this and other chalcogenide glass-formers.³ Finally, GeO_2 glass is considered where the results from recent in situ high-pressure NDIS experiments are helping to arbitrate between competing molecular dynamics models for the density-driven network collapse.

1.2 Outline Diffraction Theory

In a neutron diffraction experiment on a liquid or glassy MX_2 system, the coherent scattered intensity measured with respect to the magnitude of the scattering vector k can be represented by the total structure factor [44]

$$F(k) = c_M^2 b_M^2 [S_{MM}(k) - 1] + 2c_M c_X b_M b_X [S_{MX}(k) - 1] + c_X^2 b_X^2 [S_{XX}(k) - 1] \quad (1.1)$$

where c_α and b_α denote the atomic fraction and bound coherent scattering length of chemical species α , respectively. $S_{\alpha\beta}(k)$ is a so-called Faber-Ziman [45] partial structure factor which is related to the partial pair-distribution function $g_{\alpha\beta}(r)$ by the Fourier transform relation

³Chalcogenide glass-forming materials are those containing one or more of the chalcogen elements S, Se and Te.

$$g_{\alpha\beta}(r) = 1 + \frac{1}{2\pi^2 \rho r} \int_0^\infty dk k [S_{\alpha\beta}(k) - 1] \sin(kr), \quad (1.2)$$

where ρ is the atomic number density of the system and r is a distance in real space. The mean coordination number of atoms of type β , contained in a volume defined by two concentric spheres of radii r_1 and r_2 centred on an atom of type α , is given by

$$\bar{n}_\alpha^\beta = 4\pi \rho c_\beta \int_{r_1}^{r_2} dr r^2 g_{\alpha\beta}(r). \quad (1.3)$$

The full set of $S_{\alpha\beta}(k)$ functions for an MX_2 system can be extracted from the measured diffraction patterns by applying the NDIS method, provided that isotopes are available with a sufficiently large neutron scattering length contrast [44, 46, 47].

The total structure factor can also be expressed in terms of the Bhatia-Thornton [48] number-number, concentration-concentration and number-concentration partial structure factors denoted by $S_{\text{NN}}(k)$, $S_{\text{CC}}(k)$ and $S_{\text{NC}}(k)$, respectively. These partial structure factors are related to fluctuations (in the liquid or glass) of the number density, concentration and their cross-correlation, respectively. Equation (1.1) can be re-written as

$$F(k) = \langle b \rangle^2 [S_{\text{NN}}(k) - 1] + c_{\text{M}} c_{\text{X}} (b_{\text{M}} - b_{\text{X}})^2 \{ [S_{\text{CC}}(k)/c_{\text{M}} c_{\text{X}}] - 1 \} + 2 \langle b \rangle (b_{\text{M}} - b_{\text{X}}) S_{\text{NC}}(k) \quad (1.4)$$

where $\langle b \rangle = c_{\text{M}} b_{\text{M}} + c_{\text{X}} b_{\text{X}}$ is the average coherent neutron scattering length. The relationships between the two sets of partial structure factors are given by

$$S_{\text{NN}}(k) = c_{\text{M}}^2 S_{\text{MM}}(k) + c_{\text{X}}^2 S_{\text{XX}}(k) + 2c_{\text{M}} c_{\text{X}} S_{\text{MX}}(k), \quad (1.5)$$

$$S_{\text{CC}}(k) = c_{\text{M}} c_{\text{X}} \{ 1 + c_{\text{M}} c_{\text{X}} [S_{\text{MM}}(k) + S_{\text{XX}}(k) - 2S_{\text{MX}}(k)] \}, \quad (1.6)$$

$$S_{\text{NC}}(k) = c_{\text{M}} c_{\text{X}} \{ c_{\text{M}} [S_{\text{MM}}(k) - S_{\text{MX}}(k)] - c_{\text{X}} [S_{\text{XX}}(k) - S_{\text{MX}}(k)] \}. \quad (1.7)$$

The Fourier transforms of $S_{\text{NN}}(k)$, $S_{\text{CC}}(k)$ and $S_{\text{NC}}(k)$ are the partial pair-distribution functions $g_{\text{NN}}(r)$, $g_{\text{CC}}(r)$ and $g_{\text{NC}}(r)$, respectively. The relationships between the $g_{IJ}(r)$ ($I, J = \text{N, C}$) and $g_{\alpha\beta}(r)$ ($\alpha, \beta = \text{M, X}$) functions are given by

$$g_{\text{NN}}(r) = c_{\text{M}}^2 g_{\text{MM}}(r) + c_{\text{X}}^2 g_{\text{XX}}(r) + 2c_{\text{M}} c_{\text{X}} g_{\text{MX}}(r), \quad (1.8)$$

$$g_{\text{CC}}(r) = c_{\text{M}} c_{\text{X}} [g_{\text{MM}}(r) + g_{\text{XX}}(r) - 2g_{\text{MX}}(r)], \quad (1.9)$$

$$g_{\text{NC}}(r) = c_{\text{M}} [g_{\text{MM}}(r) - g_{\text{MX}}(r)] - c_{\text{X}} [g_{\text{XX}}(r) - g_{\text{MX}}(r)]. \quad (1.10)$$

If $b_{\text{M}} = b_{\text{X}}$ the incident neutrons in a diffraction experiment cannot distinguish between the different scattering nuclei and the measured total structure factor gives $S_{\text{NN}}(k)$ directly (see (1.4)). The corresponding Fourier transform $g_{\text{NN}}(r)$ therefore

describes the sites of the scattering nuclei and, since it cannot distinguish between the chemical species that decorate those sites, it gives information on the topological ordering. If $\langle b \rangle = 0$, however, the measured total structure factor gives $S_{CC}(k)$ directly and its Fourier transform $g_{CC}(r)$ describes the chemical ordering of the M and X atomic species. The $g_{CC}(r)$ function will have a positive or negative peak at a given distance when there is a preference for like or unlike neighbours, respectively (see (1.9)). The $g_{NC}(r)$ function describes the correlation between the sites described by $g_{NN}(r)$ and their occupancy by a given chemical species.

In practice, a diffractometer can only access a finite k -space range with a maximum cutoff value k_{\max} . Provided that sufficiently small k -values can be accessed, a reciprocal-space function such as $F(k)$ will therefore be truncated by a modification function given by $M(k) = 1$ for $k \leq k_{\max}$ and $M(k) = 0$ for $k > k_{\max}$. In consequence, the real-space information corresponding to $F(k)$ is obtained by the Fourier transform relation

$$G(r) = \frac{1}{2\pi^2 \rho r} \int_0^\infty dk k F(k) M(k) \sin(kr). \quad (1.11)$$

The desired r -space information is therefore convoluted with the Fourier transform of $M(k)$, the effect of which becomes negligible if k_{\max} is sufficiently large that $F(k)$ is featureless at higher k -values. To give smoother r -space functions, other expressions for $M(k)$ are used such as the Lorch [49] modification function where $M(k) = \sin(\pi k/k_{\max})/(\pi k/k_{\max})$ for $k \leq k_{\max}$ and $M(k) = 0$ for $k > k_{\max}$.⁴ To facilitate a like-for-like comparison between measured and molecular dynamics results, the reciprocal-space functions constructed from simulations are often Fourier transformed according to (1.11) with k_{\max} set at the experimental value.

1.3 Ionic Interaction Models for MX₂ Glass-Forming Materials

The NDIS method has been used to measure the full set of partial structure factors for molten salts with the MX₂ stoichiometry. The effect on the structure of varying the cation to anion size ratio was thereby investigated for liquid BaCl₂ [51], SrCl₂ [52], CaCl₂ [53], MgCl₂ [54], NiCl₂ [55] and ZnCl₂ [14] where the radius of Cl⁻ is 1.81 Å and the cation radii are 1.35 Å (Ba²⁺), 1.18 Å (Sr²⁺), 1.00 Å (Ca²⁺), 0.72 Å (Mg²⁺), 0.69 Å (Ni²⁺) and 0.74 Å (Zn²⁺) [56].⁵ Of these liquids, only ZnCl₂ readily forms a glass by bulk-quenching methods, and corner-sharing ZnCl₄ tetrahedra are the predominant structural motifs.

⁴A rigorous derivation of the Lorch modification function and its corresponding real-space representation is given in [50].

⁵The radii correspond to six-fold coordinated ions.

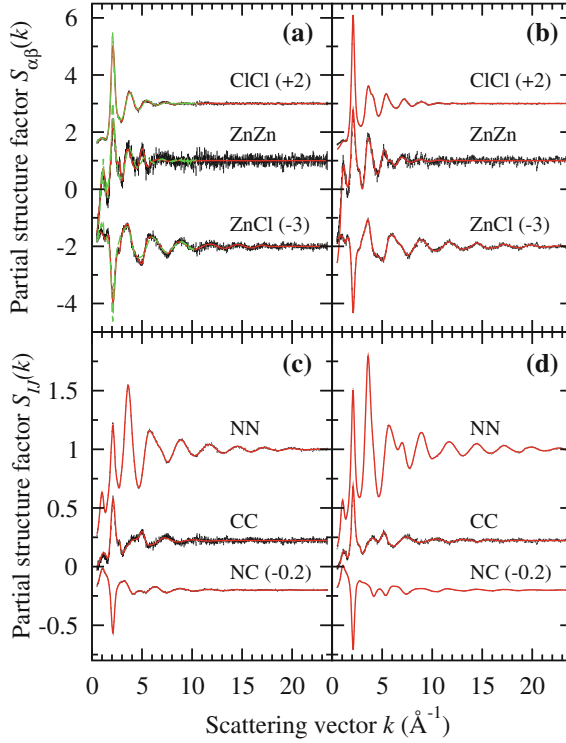


Fig. 1.1 The Faber-Ziman $S_{\alpha\beta}(k)$ ($\alpha, \beta = \text{M, X}$) and Bhatia-Thornton $S_{IJ}(k)$ ($I, J = \text{N, C}$) partial structure factors for liquid and glassy ZnCl_2 . The points with vertical (*black*) error bars are the measured functions in (a) and (c) for the liquid at 332(5) °C [16] and in (b) and (d) for the glass at 25(1) °C [15, 16]. The solid (*red*) curves are the Fourier back transforms of the corresponding partial pair-distribution functions after the unphysical oscillations at r -values smaller than the distance of closest approach between the centres of two atoms are set to the calculated limit at $r = 0$. The broken (*green*) curves in (a) are from the polarisable ion model of Sharma and Wilson [63] for the liquid at 327 °C

The full set of partial structure factors recently measured for liquid and glassy ZnCl_2 are shown in Fig. 1.1 [15, 16]. The prominent first sharp diffraction peak (FSDP) in $S_{\text{ZnZn}}(k)$ at a scattering vector $k_{\text{FSDP}} \simeq 1 \text{ \AA}^{-1}$ is a signature of structural complexity on an intermediate length scale with a periodicity given by $2\pi/k_{\text{FSDP}}$ and with a correlation length given by $2\pi/\Delta k_{\text{FSDP}}$ where Δk_{FSDP} is the full-width at half-maximum of the FSDP [57]. As shown in Fig. 1.1, the principal peaks⁶ in the Faber-Ziman partial structure factors align at a common scattering vector $k_{\text{pp}} \simeq 2.1 \text{ \AA}^{-1}$ and it follows from (1.5)–(1.7) that the principal peaks in the Bhatia-Thornton [48] partial structure factors $S_{IJ}(k)$ also align at this common position. The measured $S_{\text{NN}}(k)$ function for the liquid shows a clear ‘three-peak’ character that is not shared

⁶ A so-called principal peak or trough at $k_{\text{pp}} \simeq 2\text{--}3 \text{ \AA}^{-1}$ is a common feature in the partial structure factors for liquid and glassy materials [47].

with the other molten salts listed above, and all of the partial structure factors $S_{IJ}(k)$ ($I, J = \text{N, C}$) for both the liquid and glass display an FSDP [58, 59] e.g. there are concentration fluctuations on an intermediate length scale that will be discussed further in Sect. 1.4.3.

The experimental results for molten ZnCl_2 feature a nearest-neighbour Zn–Zn distance that is comparable to the nearest-neighbour Cl–Cl distance. This observation is not expected on the basis of a rigid ion model (RIM) for the interionic interactions in which the ions are non-deformable and the Coulomb repulsion between divalent cations is large. The experimental results for molten ZnCl_2 have therefore been attributed to a manifestation of ‘covalent’ effects in the bonding [60]. As shown by Wilson and Madden [18], however, it is possible to describe the structure of ZnCl_2 within the framework of an ionic interaction model, provided that account is taken of the anion polarisability α_X . The effect of this polarisability is shown in Fig. 1.2 where two simulations are made on an MX_2 system in which the M^{2+} and X^- ions take full formal charges but α_X is either set to zero, corresponding to a RIM, or set to 20 au, corresponding to a polarisable ion model (PIM) [61]. An FSDP develops in $S_{\text{MM}}(k)$ at $k_{\text{FSDP}} \simeq 1.2 \text{ \AA}^{-1}$ as the anion polarisability is increased to $\alpha_X = 20 \text{ au}$ and the principal peaks in all three of the Faber-Ziman partial structure factors align at a common value $k_{\text{pp}} \simeq 2 \text{ \AA}^{-1}$. The anion polarisation shields the Coulomb repulsion between divalent cations which reduces the mean M–X–M bond angle between MX_4 tetrahedra, leading to a shortening of the mean M–M distance relative to the RIM. This shielding leads to regions in which there is either an enhanced or diminished

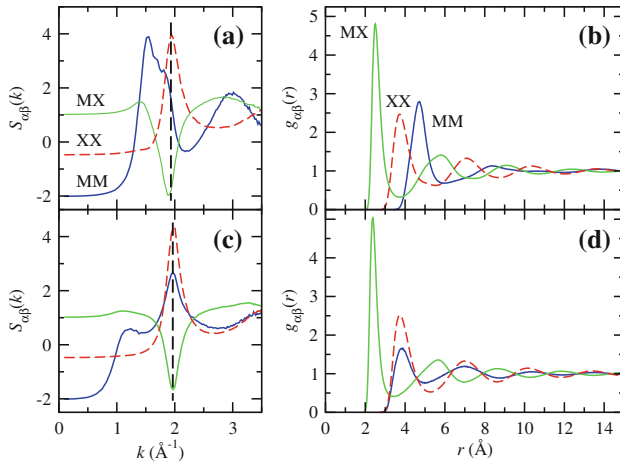


Fig. 1.2 The Faber-Ziman partial structure factors $S_{\alpha\beta}(k)$ and partial pair-distribution functions $g_{\alpha\beta}(r)$ ($\alpha, \beta = \text{M, X}$) as calculated for models using two different values for the anion polarisability α_X [61]. The curves in (a) and (b) correspond to a rigid ion model (RIM) with $\alpha_X = 0$, while the curves in (c) and (d) correspond to a polarisable ion model (PIM) with $\alpha_X = 20 \text{ au}$. The introduction of anion polarisability leads to the appearance of an FSDP in $S_{\text{MM}}(k)$ at $k_{\text{FSDP}} \simeq 1.2 \text{ \AA}^{-1}$ and to an alignment of the principal peaks in all three $S_{\alpha\beta}(k)$ functions at $k_{\text{pp}} \simeq 2 \text{ \AA}^{-1}$. The alignment of the principal peaks in (c) arises from in-phase large- r oscillations in the $g_{\alpha\beta}(r)$ functions shown in (d)

cation density relative to a RIM [62] i.e. there is a modulation of the cation-cation correlations on an intermediate length scale that gives rise to the FSDP in $S_{MM}(k)$. The $S_{\alpha\beta}(k)$ functions predicted for liquid ZnCl_2 by using a PIM with $\alpha_X = 20$ au [63] are shown in Fig. 1.1a.

On cooling a liquid to form a glass, there is a sharpening of the peaks in the measured partial structure factors in accordance with a loss of thermal disorder (Fig. 1.1). Since the FSDP is already a sharp feature and is the peak that occurs at the smallest k -value, it might be expected to dominate the large- r behaviour of the partial pair-distribution functions. This is not, however, the case as can be shown by investigating the Bhatia-Thornton partial pair-correlation functions $rh_{NN}(r) \equiv r[g_{NN}(r) - 1]$, $rh_{CC}(r) \equiv r[g_{CC}(r) - 1]$ and $rh_{NC}(r) \equiv r[g_{NC}(r) - 1]$, which enable a separation of the contributions to the structure from topological versus chemical ordering [15, 50, 64, 65]. As shown in Fig. 1.3, the measured $rh_{IJ}(r)$ functions for ZnCl_2 glass show

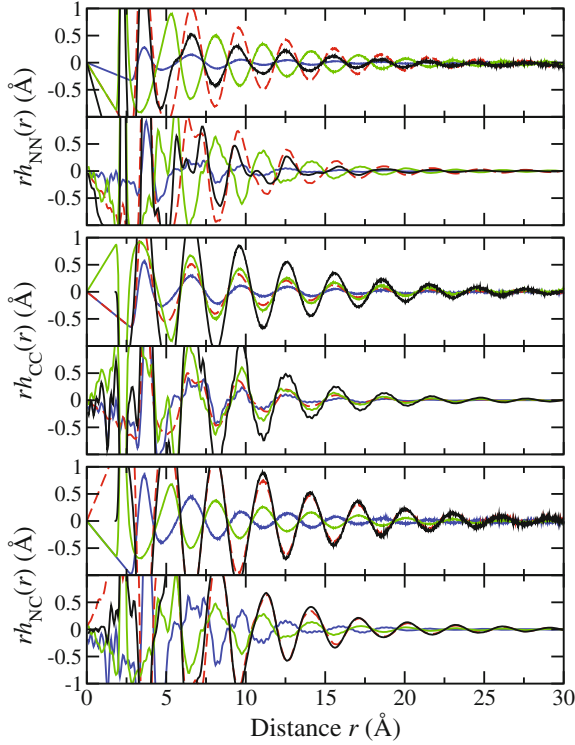


Fig. 1.3 The Bhatia-Thornton pair-correlation functions $rh_{IJ}(r)$ ($I, J = N, C$) [solid dark (black) curves] where the upper, middle and lower pairs of panels show the NN, CC and NC functions, respectively. For each pair, the upper panel gives the function obtained for a polarisable ion model (PIM) with $\alpha_X = 20$ au [20] and the lower panel gives the measured function for glassy ZnCl_2 [15, 16]. Each function is broken down into its contributions from $rh_{XX}(r)$ [broken (red) curves], $rh_{MX}(r)$ [light solid (green) curves] and $rh_{MM}(r)$ [solid (blue) curves]. The abscissa for the simulated functions are scaled by 1.98/2.09 to reflect the relative positions of the principal peak in the simulated and measured $S_{NN}(k)$ partial structure factors

large- r oscillations that extend to distances of several nanometres, well beyond the regime associated with the FSDP, with a common periodicity given by $2\pi/k_{\text{PP}}$ and a common decay length that is related to $2\pi/\Delta k_{\text{PP}}$ where Δk_{PP} is the full-width at half-maximum of a principal peak. The number of correlated ions is therefore large e.g. 4060 for a sphere of radius 30 Å in glassy ZnCl_2 where $\rho = 0.0359 \text{ Å}^{-3}$ [16]. The character of this extended range ordering is captured by the PIM with $\alpha_{\text{X}} = 20 \text{ au}$ as indicated in Fig. 1.2d by the in-phase oscillations in the $g_{\alpha\beta}(r)$ functions at large r -values, and by the $rh_{IJ}(r)$ functions illustrated in Fig. 1.3. A PIM therefore reproduces all of the main features in the structure of ZnCl_2 that are observed by experiment.

1.3.1 Simple Theory for Extended Range Ordering

The character of the extended range ordering in network glass-forming materials such as ZnCl_2 can be addressed by using simple theory. Let the pair-potential describing the interactions between two ions labelled by i and j separated by a distance r be represented by a RIM given by the expression [66]

$$\phi_{ij}(r) = \phi_{ij}^{\text{sr}}(r) + \frac{Z_i Z_j e^2}{\epsilon r} - \frac{A_{ij}}{r^6} \quad (1.12)$$

where $Z_i e$ is the charge on the i th ion, e is the elementary charge, $\epsilon \equiv 4\pi\epsilon_r\epsilon_0$, ϵ_r is the dimensionless relative dielectric constant of the medium in which the ions are embedded, and ϵ_0 is the vacuum permittivity. In this equation, $\phi_{ij}^{\text{sr}}(r)$ describes the short-ranged repulsive interactions, $\phi_{ij}^{\text{Coul}}(r) \propto r^{-1}$ describes the Coulomb interactions, and $\phi_{ij}^{\text{disp}}(r) = -A_{ij}r^{-6}$ describes the dispersion interactions where the parameter $A_{ij} (\geq 0)$ depends on the ion polarisability [67].

For this RIM, a simple power-law dependence for the ultimate decay of the pair correlation functions is expected i.e. $rh_{\text{NN}}(r) \rightarrow r^{-5}$, $rh_{\text{CC}}(r) \rightarrow r^{-9}$ and $rh_{\text{NC}}(r) \rightarrow r^{-7}$ [50, 68]. However, if the dispersion terms are absent in (1.12), then a pole analysis of the k -space solutions to the Ornstein-Zernike equations following the method of Evans and co-workers [69, 70] leads, in the case when the system density is sufficiently high, to the following expressions for the asymptotic decay of the partial pair-correlation functions [50]

$$rh_{\text{NN}}(r) \rightarrow 2|\mathcal{A}_{\text{NN}}| \exp(-a_0 r) \cos(a_1 r - \theta_{\text{NN}}), \quad (1.13)$$

$$rh_{\text{CC}}(r) \rightarrow 2c_{\text{MCX}}|\mathcal{A}_{\text{CC}}| \exp(-a_0 r) \cos(a_1 r - \theta_{\text{CC}}), \quad (1.14)$$

$$rh_{\text{NC}}(r) \rightarrow 2|\mathcal{A}_{\text{NC}}| \exp(-a_0 r) \cos(a_1 r - \theta_{\text{NC}}). \quad (1.15)$$

The $rh_{IJ}(r)$ are therefore exponentially damped oscillatory functions with a common decay length given by a_0^{-1} and a common wavelength for the oscillations given by

$2\pi/a_1$. The \mathcal{A}_{IJ} are complex numbers with amplitudes related by $|\mathcal{A}_{NN}||\mathcal{A}_{CC}| = |\mathcal{A}_{NC}|^2$ and the phases are related by $\theta_{NN} + \theta_{CC} = 2\theta_{NC}$. Equations (1.13)–(1.15) also hold for binary mixtures of hard-spheres having different diameters, i.e. when both the Coulomb and dispersion terms are absent from (1.12), where the common wavelength of oscillation is set by one or other of the hard sphere sizes depending on the thermodynamic conditions [71]. The effect on (1.13)–(1.15) of introducing anion polarisability has yet to be fully explored.

1.3.2 Relative Fragility of Tetrahedral Glass-Forming MX_2 Liquids

A systematic variation of the anion polarisability α_X within a PIM has been used to investigate the relative “fragility” of network glass-forming MX_2 liquids in which the predominant structural motifs are MX_4 tetrahedra [61]. The fragility is a measure of the rate at which the dynamical properties of a liquid change on approaching the glass transition temperature T_g and can be quantified in terms of a fragility index $m = d \log_{10} \eta / d (T_g/T) |_{T=T_g}$ where η is the liquid viscosity and T is the absolute temperature [72, 73]. Figure 1.4a shows the measured relation between

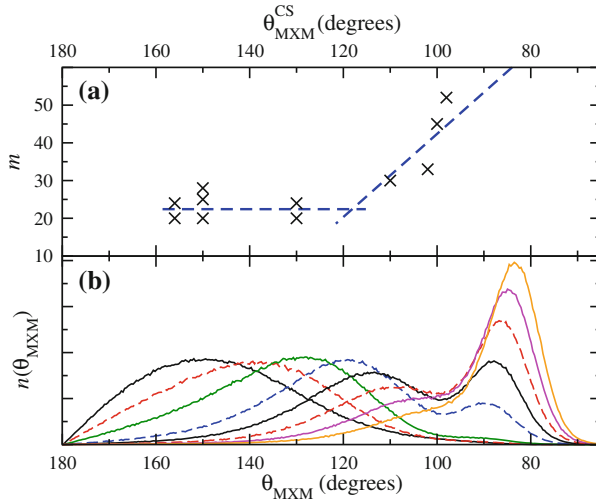


Fig. 1.4 **a** The dependence of the measured fragility index m on the M–X–M bond angle for corner-sharing tetrahedra $\theta_{\text{MXM}}^{\text{CS}}$ for a series of MX_2 network glass-forming materials. The measured $\theta_{\text{MXM}}^{\text{CS}}$ values correspond, from left to right, to BeF_2 [77], SiO_2 [78], GeO_2 [78], ZnCl_2 [77], GeS_2 [79], ZnBr_2 (estimated) and GeSe_2 [59]. The fragility values are taken from [73–76]. **b** The M–X–M bond angle distribution $n(\theta_{\text{MXM}})$ as calculated using a polarisable ion model (PIM) where the curves, appearing from left to right, correspond to anion polarisability α_X values of 0, 5, 10, 15, 17.5, 20, 22.5 and 25 au, respectively. The figure is taken from Wilson and Salmon [61]

m [73–76] and the mean M–X–M bond angle for corner-sharing MX_4 tetrahedra $\theta_{\text{MXM}}^{\text{CS}}$ [59, 77–79]. The fragility is small and approximately invariant for large $\theta_{\text{MXM}}^{\text{CS}}$ values, characteristic of networks dominated by corner-sharing units in systems like BeF_2 , SiO_2 and GeO_2 [77, 78], but increases when $\theta_{\text{MXM}}^{\text{CS}}$ reduces below $\simeq 120^\circ$ and edge-sharing units become numerous in systems like GeS_2 and GeSe_2 [59, 79]. The molecular dynamics simulations also show this trend, where the M–X–M bond angle distribution $n(\theta_{\text{MXM}})$ for different α_X values is shown in Fig. 1.4(b) and the associated fragility was assessed from the temperature dependence of the cation self-diffusion coefficient [61]. As α_X is increased above ~ 15 au, the fragility increases as a second peak due to edge-sharing units appears in $n(\theta_{\text{MXM}})$ at an angle smaller than the peak associated with $\theta_{\text{MXM}}^{\text{CS}}$. This trend towards increasing fragility with increasing fraction of edge-sharing motifs is also anticipated for other glass-forming liquids [61].

The relative fragility of tetrahedral MX_2 network glass-forming materials manifests itself in the relative importance of the FSDP versus the principal peak in the measured $S_{\text{NN}}(k)$ functions [59, 65]. For example, in the relatively fragile glass-forming system ZnCl_2 the anion packing fraction in the glass is large at 0.647(9) and the mean inter-tetrahedral M–X–M bond angle is 111° , whereas in the strong glass-forming system GeO_2 the anion packing fraction in the glass is much smaller at 0.495(5) and the mean M–X–M bond angle is larger at $132(2)^\circ$. These differences between dense and more open networks of tetrahedra lead to a principal peak in $S_{\text{NN}}(k)$ that is a more prominent feature than the FSDP for more fragile glass-formers, with the converse relation holding for strong glass-formers. Hence, there is competition between the intermediate and extended range ordering in these MX_2 materials that is won by the latter with increasing density.

1.4 Covalent Effects in MX_2 Glass-Forming Materials: Structure of Liquid and Glassy GeSe_2

In Sect. 1.3 ‘ionic’ network glass-forming systems were considered, where the properties of materials like ZnCl_2 can be reproduced by using an interaction model based on discrete closed-shell ions with integer charges i.e. there was no need to consider ‘covalent’ interactions that arise from the formation of chemical bonds in which pairs of electrons are shared between atoms. Indeed, many material properties that have been attributed to ‘covalency’ may in fact be explained in terms of ‘ionic’ interactions provided that effects such as polarisation, compression and deformation are taken into explicit account [19]. We now consider the prototypical network glass-forming material GeSe_2 where the small electronegativity difference between Ge and Se and the observation of broken chemical order precludes the successful employment of an ionic interaction model, necessitating a first-principles molecular dynamics approach [35, 37].

1.4.1 Diffraction Results for Liquid and Glassy GeSe_2

The NDIS method has been used to measure the full set of partial structure factors for liquid GeSe_2 at 784(3) °C and for glassy GeSe_2 at 26(1) °C [21–23]. Several of the main results are presented in the following, while a more complete discussion of these results in the context of other experimental work on liquids and glasses in the binary Ge-Se system is given elsewhere [47, 80].

The Faber-Ziman $S_{\alpha\beta}(k)$ and corresponding $g_{\alpha\beta}(r)$ functions are shown in Figs. 1.5, 1.6 and 1.7, and the Bhatia-Thornton $S_{IJ}(k)$ functions are shown in

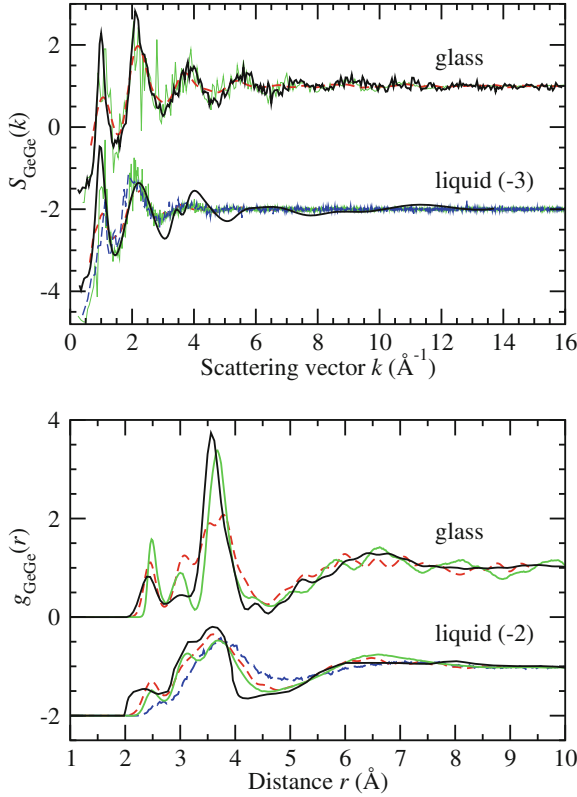
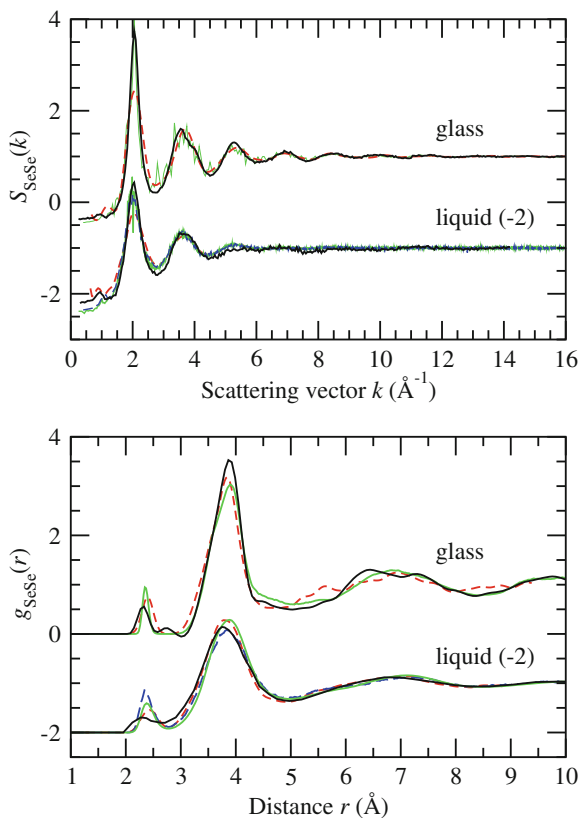


Fig. 1.5 The measured and simulated $S_{\text{GeGe}}(k)$ and $g_{\text{GeGe}}(r)$ functions for liquid and glassy GeSe_2 . The dark solid (black) curves give the measured functions for the liquid [21] and glass [22], where a spline fit to the liquid state $S_{\text{GeGe}}(k)$ function is shown for clarity of presentation. For the liquid, the light broken (red) curves show the LDA results of Cobb and Drabold [25], the dark broken (blue) curves show the LDA results of Massobrio et al. [30], and the light solid (green) curves show the BLYP results of Micoulaut et al. [39]. For the glass, the broken (red) curves show the LDA results of Zhang and Drabold [29] and the light solid (green) curves show the BLYP results of Massobrio and co-workers [87]

Fig. 1.6 The measured and simulated $S_{\text{SeSe}}(k)$ and $g_{\text{SeSe}}(r)$ functions for liquid and glassy GeSe_2 . The dark solid (black) curves give the measured functions for the liquid [21] and glass [22]. For the liquid, the light broken (red) curves show the LDA results of Cobb and Drabold [25], the dark broken (blue) curves show the LDA results of Massobrio et al. [30], and the light solid (green) curves show the BLYP results of Micoulaut et al. [39]. For the glass, the broken (red) curves show the LDA results of Zhang and Drabold [29] and the light solid (green) curves show the BLYP results of Massobrio and co-workers [87]

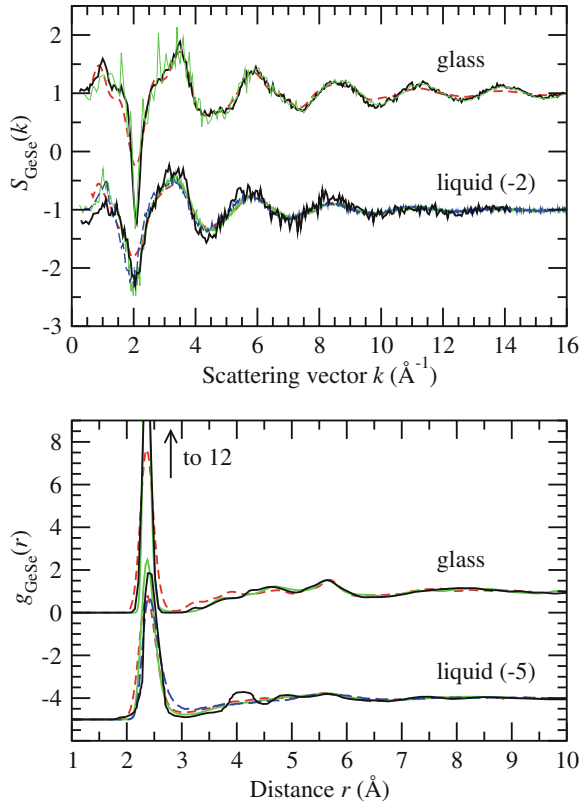


Figs. 1.8, 1.9 and 1.10.⁷ The overall features in the measured functions are similar to those observed for liquid and glassy ZnCl_2 as befits a material with a structure that is also based predominantly on MX_4 tetrahedra. For example, a prominent FSDP is observed in the partial structure factor describing the pair-correlations between the more electropositive chemical species i.e. in $S_{\text{GeGe}}(k)$ at $k_{\text{FSDP}} \simeq 1 \text{ \AA}^{-1}$; an FSDP also manifests itself as a feature in all three of the $S_{IJ}(k)$ functions; the principal peaks in the $S_{\alpha\beta}(k)$ and $S_{IJ}(k)$ functions share a common position which leads in the case of the glass to prominent extended range ordering [15, 50]; and $S_{\text{NN}}(k)$ has the same ‘three-peak’ character as shown for ZnCl_2 (Fig. 1.1). There are, however, subtle but important differences in structure, including clear evidence for homopolar bonds.

For the liquid, the main peaks in $g_{\text{GeSe}}(r)$ and $g_{\text{SeSe}}(r)$ occur at 2.42(2) and 3.75(2) \AA , respectively, giving a Ge–Se:Se–Se distance ratio of 0.645(6) as compared

⁷The r -space functions for the liquid were obtained from a maximum entropy analysis in which homopolar bonds were not excluded. Those for the glass were obtained from a procedure aimed at removing the effect in r -space of the modification function $M(k)$. A more complete discussion is given in [21, 23, 80].

Fig. 1.7 The measured and simulated $S_{\text{GeSe}}(k)$ and $g_{\text{GeSe}}(r)$ functions for liquid and glassy GeSe_2 . The dark solid (black) curves give the measured functions for the liquid [21] and glass [22]. For the liquid, the light broken (red) curves show the LDA results of Cobb and Drabold [25], the dark broken (blue) curves show the LDA results of Massobrio et al. [30], and the light solid (green) curves show the BLYP results of Micoulaut et al. [39]. For the glass, the broken (red) curves show the LDA results of Zhang and Drabold [29] and the light solid (green) curves show the BLYP results of Massobrio and co-workers [87]



to a ratio of $\sqrt{8/3} = 0.612$ for regular GeSe_4 tetrahedra. This ratio and the Ge–Se coordination number $\bar{n}_{\text{Ge}}^{\text{Se}} = 3.5(2)$ are consistent with the presence in the melt of a large number of distorted tetrahedral GeSe_4 motifs. In comparison, for the glass the main peaks in $g_{\text{GeSe}}(r)$ and $g_{\text{SeSe}}(r)$ occur at 2.36(2) and 3.89(2) Å, respectively, giving a Ge–Se:Se–Se distance ratio of 0.607(6), and $\bar{n}_{\text{Ge}}^{\text{Se}} = 3.7(1)$ i.e. the GeSe_4 motifs in the glass appear to be more regular than in the liquid.

In the high-temperature crystalline phase of GeSe_2 [81] there are equal numbers of both corner-sharing (CS) and edge-sharing (ES) tetrahedra and each Ge atom in a CS or ES tetrahedron has three or four nearest-neighbouring Ge atoms giving a Ge–Ge coordination number $\bar{n}_{\text{Ge}}^{\text{Ge}} = 3.5$. The Ge–Ge distance for ES tetrahedra is the shortest at 3.049 Å and the next largest distance is 3.508 Å. The measured $g_{\text{GeGe}}(r)$ functions for both the liquid and glass also support the existence of substantial fractions of both CS and ES tetrahedra. For the liquid, ES motifs manifest themselves by a short low- r cutoff value of $\simeq 2.8$ Å for the first main peak in $g_{\text{GeGe}}(r)$ and by the relatively small coordination number for this peak of $\bar{n}_{\text{Ge}}^{\text{Ge}} = 2.9(3)$ [21, 80]. For the glass, ES motifs show themselves by a peak in $g_{\text{GeGe}}(r)$ at 3.02(2) Å with a coordination number $\bar{n}_{\text{Ge}}^{\text{Ge}} = 0.34(5)$. If the glass does not contain extended chains of ES units then this

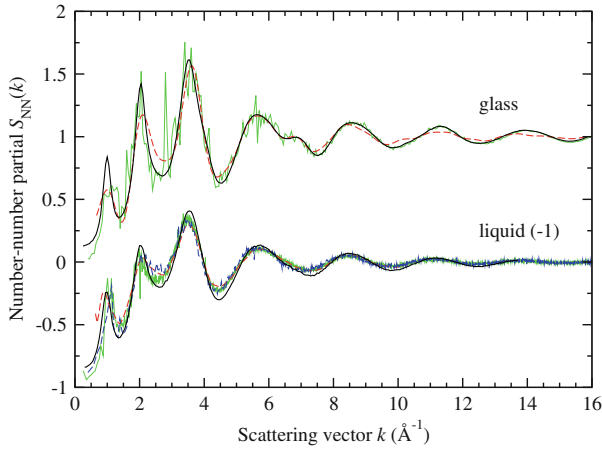


Fig. 1.8 The measured and simulated $S_{NN}(k)$ functions for liquid and glassy GeSe_2 . The dark solid (black) curves give the measured functions for the liquid [21] and glass [22]. For the liquid, the light broken (red) curves show the LDA results of Cobb and Drabold [25], the dark broken (blue) curves show the LDA results of Massobrio et al. [30], and the light solid (green) curves show the BLYP results of Micoulaut et al. [39]. For the glass, the broken (red) curves show the LDA results of Zhang and Drabold [29] and the light solid (green) curves show the BLYP results of Massobrio and co-workers [87]

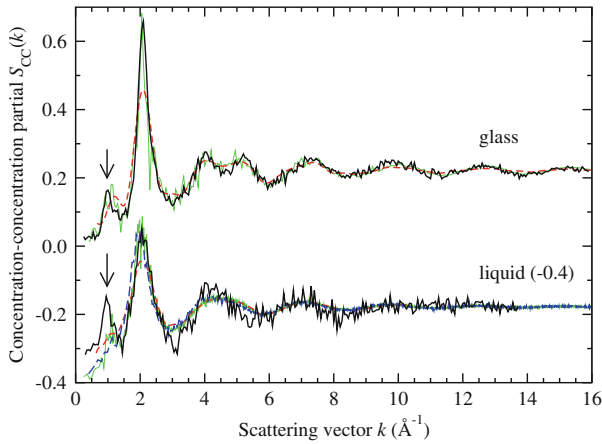


Fig. 1.9 The measured and simulated $S_{CC}(k)$ functions for liquid and glassy GeSe_2 . The dark solid (black) curves give the measured functions for the liquid [21] and glass [22]. For the liquid, the light broken (red) curves show the LDA results of Cobb and Drabold [25], the dark broken (blue) curves show the LDA results of Massobrio et al. [30], and the light solid (green) curves show the BLYP results of Micoulaut et al. [39]. For the glass, the broken (red) curves show the LDA results of Zhang and Drabold [29] and the light solid (green) curves show the BLYP results of Massobrio and co-workers [87]. The vertical arrows point to the FSDP

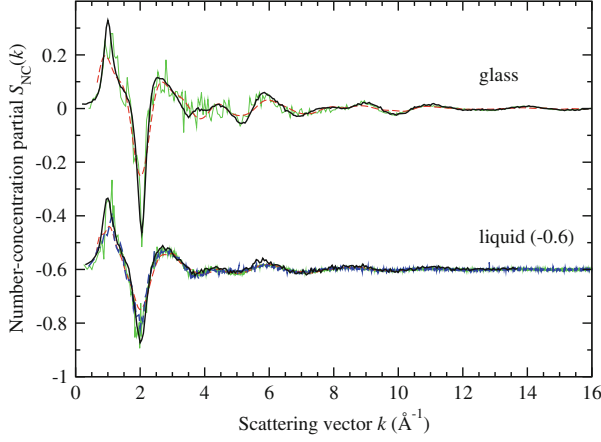


Fig. 1.10 The measured and simulated $S_{NC}(k)$ functions for liquid and glassy GeSe_2 . The dark solid (black) curves give the measured functions for the liquid [21] and glass [22]. For the liquid, the light broken (red) curves show the LDA results of Cobb and Drabold [25], the dark broken (blue) curves show the LDA results of Massobrio et al. [30], and the light solid (green) curves show the BLYP results of Micoulaut et al. [39]. For the glass, the broken (red) curves show the LDA results of Zhang and Drabold [29] and the light solid (green) curves show the BLYP results of Massobrio and co-workers [87]

coordination number can be written as $\bar{n}_{\text{Ge}}^{\text{Ge}} = (N_{\text{Ge,ES}} \times 1) / N_{\text{Ge}}$ where $N_{\text{Ge,ES}}$ is the number of Ge atoms in ES units and N_{Ge} is the total number of Ge atoms. Hence 34(5) % of the Ge atoms in the glass are involved in ES motifs.

As shown by the $g_{\alpha\beta}(r)$ functions of Figs. 1.5 and 1.6, there is clear evidence for a substantial number of Ge–Ge and Se–Se homopolar bonds in both the liquid and glass, with measured Ge–Ge distances of 2.33(3) Å (liquid) and 2.42(2) Å (glass) and with measured Se–Se distances of 2.30(2) Å (liquid) and 2.32(2) Å (glass). These distances are comparable to the Ge–Ge contact distances in liquid GeSe and amorphous Ge (2.36–2.47 Å) and to the Se–Se contact distances in liquid GeSe and Se (2.34–2.35 Å) [80]. For the liquid, the corresponding Ge–Ge and Se–Se coordination numbers are 0.25(10) and 0.23(5), respectively, and since $\bar{n}_{\text{Ge}}^{\text{Se}} = 3.5(2)$ the total Ge and Se coordination numbers are $\bar{n}_{\text{Ge}} \equiv \bar{n}_{\text{Ge}}^{\text{Se}} + \bar{n}_{\text{Ge}}^{\text{Ge}} = 3.8(2)$ and $\bar{n}_{\text{Se}} \equiv \bar{n}_{\text{Se}}^{\text{Ge}} + \bar{n}_{\text{Se}}^{\text{Se}} = 2.0(1)$. For the glass, the corresponding Ge–Ge and Se–Se coordination numbers are 0.25(5) and 0.20(5), respectively, and since $\bar{n}_{\text{Ge}}^{\text{Se}} = 3.7(1)$ the total Ge and Se coordination numbers are $\bar{n}_{\text{Ge}} = 4.0(1)$ and $\bar{n}_{\text{Se}} = 2.05(7)$.⁸ These \bar{n}_{Ge} and \bar{n}_{Se} values imply that Ge and Se are, within the experimental error, fourfold and twofold coordinated

⁸For the glass, an estimate of the number of Ge atoms in CS tetrahedra $N_{\text{Ge,CS}}$ can be obtained by taking $N_{\text{Ge}} = N_{\text{Ge,ES}} + N_{\text{Ge,CS}} + N_{\text{Ge,homo}}$ where $N_{\text{Ge,homo}}$ is the number of Ge atoms in homopolar Ge–Ge bonds (see Appendix). If there are no extended chains of ES units then the corresponding coordination number $\bar{n}_{\text{Ge}}^{\text{Ge}} = (N_{\text{Ge,ES}} \times 1) / N_{\text{Ge}} = 0.34(5)$ and if homopolar bonds form only in pairs then the corresponding coordination number $\bar{n}_{\text{Ge}}^{\text{Ge}} = (N_{\text{Ge,homo}} \times 1) / N_{\text{Ge}} = 0.25(5)$. Hence $N_{\text{Ge,CS}} / N_{\text{Ge}} = 1 - 0.34(5) - 0.25(5) = 0.41(7)$ such that $N_{\text{Ge,ES}} / N_{\text{Ge,CS}} = 0.34(5) / 0.41(7) = 0.83(16)$ [23].

in both the liquid and glass i.e. both chemical species have a full outer shell of eight electrons. The observation by the NDIS method of homopolar bonds in GeSe_2 glass is consistent with the findings from Raman, Mössbauer and x-ray emission spectroscopy experiments [23, 82, 83], and the fraction of homopolar bonds is in agreement with an estimate based on the law of mass action (see Appendix).

As shown in Figs. 1.8, 1.9 and 1.10, the overall features in a given Bhatia-Thornton $S_{IJ}(k)$ function are similar for both liquid and glassy GeSe_2 , but the peaks for the glass are generally sharper than for the liquid in accordance with a loss of thermal disorder. A notable feature is the appearance of an FSDP in $S_{CC}(k)$ at $k_{\text{FSDP}} \simeq 1 \text{ \AA}^{-1}$ which, from inspection of (1.6) and Figs. 1.5, 1.6 and 1.7, arises predominantly from the Ge–Ge correlations. The significance of an FSDP in $S_{CC}(k)$ will be discussed in Sect. 1.4.3.

1.4.2 First-Principles Molecular Dynamics Simulations of Liquid and Glassy GeSe_2

The GeSe_2 system has been the subject of extensive first-principles molecular dynamics simulations in which the electronic structure is taken into explicit account, as befits a material in which the electronegativities of the different chemical species are similar and the bonding takes an iono-covalent character [24–40].

Drabold and co-workers used an electronic-structure scheme within the local density approximation (LDA) for the exchange and correlation energy which does not evolve self-consistently with the atomic motion, together with a minimal basis set [24, 25, 29]. As illustrated in Figs. 1.5, 1.6, 1.7, 1.8, 1.9 and 1.10 the models do, however, reproduce many of the features in the NDIS results for the liquid and glass such as homopolar Ge–Ge and Se–Se bonds and the appearance of an FSDP in $S_{CC}(k)$.

Massobrio and co-workers first investigated liquid GeSe_2 by using fully self-consistent LDA calculations, but it was found that this approach led to structures that were too disordered (Figs. 1.5, 1.6, 1.7, 1.8, 1.9 and 1.10). This limitation was attributed to an underestimation of the ionic contribution to the bonding [26–28, 30] which led inter alia to use of the Perdew and Wang [84] generalised gradient approximation for the exchange and correlation energy, and to improved agreement with experiment [26–28, 30, 37]. Nevertheless, discrepancies remained that were particularly noticeable with regards to the Ge–Ge and concentration-concentration partial pair-correlation functions. These limitations led to an employment of the Becke, Lee, Yang and Parr (BLYP) generalised gradient approximation for the exchange and correlation energy [85, 86] to further enhance a localised distribution of the valence electrons. The results from this approach are leading to good agreement with the NDIS results for the liquid (Figs. 1.5, 1.6, 1.7, 1.8, 1.9 and 1.10) and to diffusion coefficients that are in better agreement with those expected from experiment [36, 39].

The procedure used to quench a liquid to the glass is expected to affect the resultant structure, especially since the simulated quench rates are many orders of magnitude faster than experimental ones. Massobrio and Pasquarello [34] devised a protocol that leads to marked differences between the glass and liquid structures, but it transpired that use of the NVT ensemble with a number density set at the measured value $\rho = 0.034 \text{ \AA}^{-3}$ led to a marked overpressure of $\sim 1 \text{ GPa}$ [40]. This problem was addressed by increasing the size of the simulation box to reduce the number density to $\rho = 0.0326 \text{ \AA}^{-3}$, essentially eliminating the overpressure and leading to a structure that is in better agreement with experiment [40]. It was later found that this revised density is in excellent agreement with the value $\rho = 0.0324(1) \text{ \AA}^{-3}$ obtained from recent measurements on GeSe_2 glass [87]. As shown in Figs. 1.5, 1.6, 1.7, 1.8, 1.9 and 1.10, the combined use of the quench-rate protocol, revised number density and BLYP functional is now capturing all of the main features found from the NDIS experiments on GeSe_2 glass under ambient conditions [87]. It will be interesting to see whether this latest model yields a vibrational density of states for the ambient pressure glass that is in good agreement with experiment [88, 89].

1.4.3 Concentration Fluctuations on an Intermediate Length Scale

An FSDP in $S_{CC}(k)$ is observed for the liquid and glassy forms of GeSe_2 (Fig. 1.9) and ZnCl_2 (Fig. 1.1) and for several other MX_2 network glass-forming materials [31, 58, 59]. This peak has been a source of controversy because it was not predicted from previous investigations of these materials by using classical molecular dynamics simulations or integral-equation calculations [90–93]. Also, if these systems can be treated as purely ionic materials containing point-like cations and anions, then $S_{CC}(k)$ is related to the charge-charge partial structure factor $S_{ZZ}(k)$ by the equation $S_{CC}(k) = c_{MX} S_{ZZ}(k)$ such that an FSDP in $S_{CC}(k)$ implies a non-uniformity in the charge distribution on an intermediate length scale [58].

First-principles molecular dynamics simulations of liquid or amorphous GeSe_2 , SiSe_2 and SiO_2 have been undertaken to examine the issue of concentration versus charge fluctuations on an intermediate length scale [31, 37]. In this work $S_{CC}(k)$, which depends on the atomic positions, was calculated separately from $S_{ZZ}(k)$, which depends on the valence-electron density. No FSDP was found for $S_{ZZ}(k)$ i.e. no evidence was found for charge fluctuations on an intermediate length scale. This led to a proposal for three classes of network-forming materials. Class I systems have perfect chemical order and no FSDP in $S_{CC}(k)$, class II systems have a moderate number of defects in an otherwise chemically ordered network and an FSDP in $S_{CC}(k)$, and class III systems have a large degree of chemical disorder, feature a rich variety of structural motifs, and show no FSDP in $S_{CC}(k)$ [31].

The appearance of charge neutrality on an intermediate length scale provides an important constraint on the network connectivity leading to these different network

types. For example, in chemically ordered class I systems like SiO_2 the network is made from the same type of charge-neutral motif and concentration fluctuations need not occur on an intermediate range. In class II materials like GeSe_2 and SiSe_2 , however, there is a moderate number of defects leading to a variability of M-centred structural motifs with different charges. These motifs must form a network in which there is charge neutrality on the length scale of a few structural motifs, leading to an arrangement with a non-uniform distribution of M-atoms i.e. to the appearance of concentration fluctuations on an intermediate length scale. By comparison, in more chemically disordered class III systems, the network structure is broken-up and the intermediate range order disappears such that the FSDP becomes a less prominent feature in $F(k)$ and disappears from $S_{\text{CC}}(k)$.⁹

Liquid and glassy ZnCl_2 are chemically ordered materials [14–16] and, according to the above, should therefore be categorised as class I network-forming materials. NDIS experiments show, however, that there is an FSDP in $S_{\text{CC}}(k)$ (Fig. 1.1), and edge-sharing tetrahedra are indicated by molecular dynamics [94] and RMC [16, 17] models and by Raman spectroscopy [95]. Edge-sharing motifs containing mis-coordinated atoms (i.e. those not satisfying the ‘8-N’ rule) are primarily responsible for the FSDP in $S_{\text{CC}}(k)$ for GeSe_2 [33], and the majority of Si atoms in SiSe_2 are involved in edge-sharing conformations [37, 96]. In contrast, the measured partial structure factors for glassy SiO_2 do not show an FSDP in $S_{\text{CC}}^{\text{BT}}(k)$ [97] and the network, based on corner-sharing SiO_4 tetrahedra, is chemically-ordered [98]. On the other hand, glassy GeO_2 also forms a chemically-ordered network based on corner-sharing GeO_4 tetrahedra, but in this case the measured partial structure factors *do* show a small FSDP in $S_{\text{CC}}^{\text{BT}}(k)$ [65, 99]. For this material, a first-principles molecular dynamics model also shows a small FSDP in $S_{\text{CC}}^{\text{BT}}(k)$ and, although its origin is unknown, it is not related to coordination defects since they were not present in the model [100].

This evidence suggests a revised definition for class I and II network-forming MX_2 materials along the lines suggested in [101]. Class I systems form chemically ordered corner-sharing networks, class II systems form networks that incorporate both corner- and edge-sharing motifs, and class III systems form networks that are chemically disordered. Class I and II networks may both exhibit an FSDP in $S_{\text{CC}}^{\text{BT}}(k)$ where, in the case of class II systems, this feature originates primarily from edge-sharing motifs that may contain structural defects. In the case of class I systems, however, the FSDP does not originate from the fourfold rings associated with these edge-sharing conformations. Thus, the concentration-concentration partial structure factor is proving to be a sensitive probe of the ordering in network glass-forming materials [17].

⁹In [31] a first-principles molecular dynamics model for liquid GeSe_2 using the Perdew and Wang generalised gradient approximation was given as an example of a class III system. More recent models of this material using the BLYP generalised gradient approximation reduce the chemical disorder and produce a more pronounced FSDP in $S_{\text{CC}}(k)$, in better accord with experiment (Fig. 1.9). The measured FSDP in $S_{\text{CC}}(k)$ for glassy GeSe_2 is accurately reproduced by first-principles molecular dynamics simulations using the BLYP generalised gradient approximation (Fig. 1.9).

1.5 Density-Driven Mechanisms of Network Collapse in MX_2 Glasses: Structure of GeO_2 Under Pressure

The structural changes in glasses and liquids induced by high-pressure and/or high-temperature conditions can have a profound effect on their physico-chemical properties [72, 98, 102, 103]. A notable example is provided by so-called polyamorphic transitions, where the variation of pressure and/or temperature leads to an abrupt transformation between two phases having identical compositions but different densities [72, 98, 102–107]. It is therefore important to unravel the mechanisms by which these transformations occur in order to establish the underlying relationships to the network structure. This is not, however, a straightforward task as competing processes are often at work. For example, the compression of a network formed by corner-sharing tetrahedral MO_4 motifs could lead to a retention of these motifs but to a change in the distribution of primitive ring sizes,¹⁰ as indicated by the ring statistics for different density polymorphs of crystalline SiO_2 [108]. Compression may, however, also lead to an alteration in character of the network-forming motifs as they transform to higher-coordinated polyhedra such as MO_5 square pyramids or MO_6 octahedra. In the following, the case example of GeO_2 glass under cold-compression (i.e. pressurisation at constant temperature) will be considered. The results highlight the usefulness of NDIS in helping to test the efficacy of the different molecular dynamics models that have been proposed for this material, and demonstrate the need for atomic interaction models that can be reliably transferred to high-pressure conditions.

Figure 1.11 shows the difference functions $\Delta F_{\text{Ge}}(k)$ and $\Delta F_{\text{O}}(k)$ as measured for GeO_2 glass at pressures up to 8 GPa by employing the in situ high-pressure NDIS method [109]. In these experiments, the total structure factors $F(k)$ are measured for two samples that are identical in every respect, except for the isotopic enrichment of the Ge atoms. These $F(k)$ functions are then subtracted in order to simplify the complexity of correlations associated with a single measurement [110, 111]. For example, $\Delta F_{\text{Ge}}(k)$ is given by

$$\Delta F_{\text{Ge}}(k)/\text{barn} = 0.124(3) [S_{\text{GeO}}(k) - 1] + 0.081(2) [S_{\text{GeGe}}(k) - 1] \quad (1.16)$$

and, because the contribution from $S_{\text{OO}}(k)$ has been eliminated, it gives site-specific information on the germanium atom correlations. Similarly, $\Delta F_{\text{O}}(k)$ is given by

$$\Delta F_{\text{O}}(k)/\text{barn} = 0.0875(5) [S_{\text{GeO}}(k) - 1] + 0.1497(2) [S_{\text{OO}}(k) - 1] \quad (1.17)$$

and, because the contribution from $S_{\text{GeGe}}(k)$ has been eliminated, it gives complementary site-specific information on the oxygen atom correlations. The corresponding

¹⁰A ring is a measure of the network topology and is a closed path usually chosen to pass along the bonds which connect nearest-neighbour atoms. A ring is primitive if it cannot be decomposed into smaller rings [108].

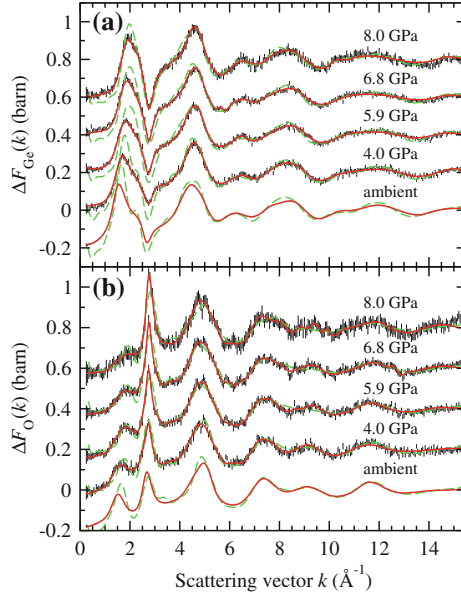


Fig. 1.11 The pressure dependence of the difference functions **a** $\Delta F_{\text{Ge}}(k)$ and **b** $\Delta F_{\text{O}}(k)$ for GeO_2 glass at ambient temperature [109]. The vertical bars give the statistical errors on the measured data points, the solid (red) curves give the Fourier transforms of the corresponding real-space functions shown in Fig. 1.12, and the broken (green) curves give the molecular dynamics results obtained by using the DIPPIM. The high-pressure data sets have been shifted vertically for clarity of presentation. The figure is adapted from Wezka et al. [109]

real-space functions $\Delta G_{\text{Ge}}(r)$ and $\Delta G_{\text{O}}(r)$ are obtained by replacing $S_{\alpha\beta}(k)$ by $g_{\alpha\beta}(r)$ in (1.16) and (1.17), respectively, and are shown in Fig. 1.12.

The first peak in both $\Delta G_{\text{Ge}}(r)$ and $\Delta G_{\text{O}}(r)$ originates from the Ge–O correlations, and the dependence on pressure of the corresponding Ge–O bond distance r_{GeO} and coordination number $\bar{n}_{\text{Ge}}^{\text{O}}$ is shown in Fig. 1.13. The second peaks in these functions originate from nearest-neighbour Ge–Ge and O–O correlations, respectively. The dependence on pressure of the corresponding peak positions r_{GeGe} and r_{OO} is also shown in Fig. 1.13, along with the O–O coordination number $\bar{n}_{\text{O}}^{\text{O}}$ which was obtained by assuming minimal overlap between the O–O and Ge–O correlations as observed under ambient conditions [99]. The resolution of these peaks, which is made possible by using the difference function method, also enables an estimate of the mean O–Ge–O and Ge–O–Ge bond angles as deduced from the measured nearest-neighbour distances according to $\cos(\theta_{\text{OGeO}}) = 1 - r_{\text{OO}}^2/2r_{\text{GeO}}^2$ and $\cos(\theta_{\text{GeOGe}}) = 1 - r_{\text{GeGe}}^2/2r_{\text{GeO}}^2$. The results are plotted in Fig. 1.14 as a function of the reduced density ρ/ρ_0 where ρ_0 is the value of the number density ρ at ambient pressure. This reduced density facilitates a ready comparison with the bond angles measured by diffraction experiments on the α -quartz polymorph of crystalline GeO_2 [112, 113]. The density-to-pressure conversion was made using the equation of state measured by Hong et al. [114].

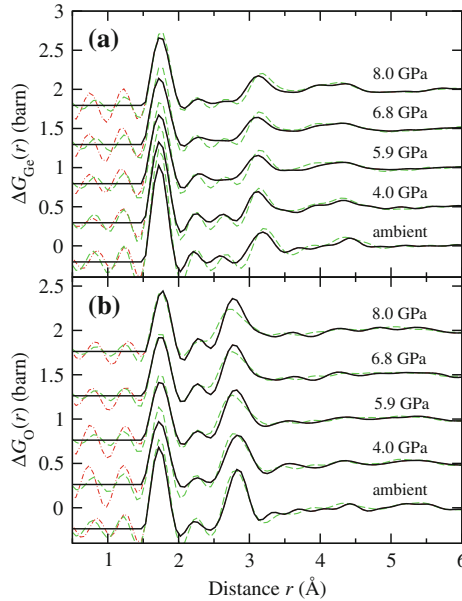


Fig. 1.12 The solid (black) curves show the difference functions **a** $\Delta G_{\text{Ge}}(r)$ and **b** $\Delta G_{\text{O}}(r)$ obtained by spline fitting and Fourier transforming the measured reciprocal-space functions shown in Fig. 1.11 at pressures ranging from ambient to 8 GPa. The chained (red) curves show the oscillations at r -values smaller than the distance of closest approach between two atoms. The broken (green) curves give the molecular dynamics results obtained by Fourier transforming the simulated functions shown in Fig. 1.11 after applying the same maximum cutoff k_{max} as for the neutron diffraction data. The high-pressure data sets have been shifted vertically for clarity of presentation. The figure is adapted from Wezka et al. [109]

In Figs. 1.11, 1.12, 1.13 and 1.14, the diffraction results are compared to molecular dynamics simulations made using the so-called DIPole-Polarisable Ion Model (DIPPIM) where the atomic interaction potentials include dipole-polarisation effects [43, 109, 115]. The potentials were parameterised using ab initio simulations as opposed to experimental results and should therefore be largely unbiased in their predictions of the glass structure. The DIPPIM is the only model currently available that gives, for a single set of parameters, a good account of both the structural and vibrational properties of glassy GeO_2 at ambient pressure along with the dynamical properties of liquid GeO_2 at elevated temperatures [115]. The ambient pressure glass was obtained by a quench-from-the-melt procedure, and the high-pressure configurations were generated by a cold-compression procedure [41] in which the cell lengths and particle positions were rescaled for each new density. The methodology did not reproduce the measured equation of state [43], so the simulations were made with the glass density set at measured values [109].

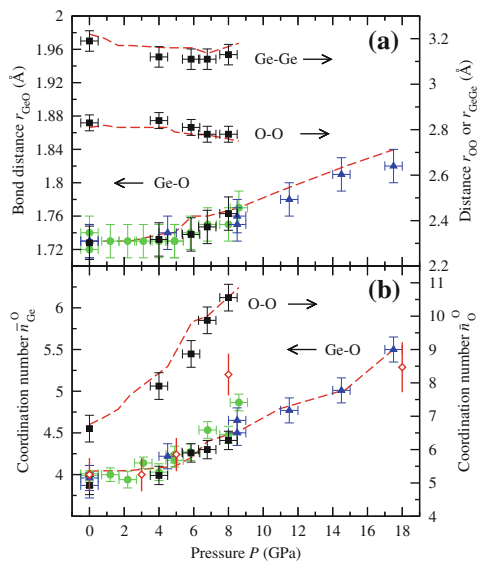


Fig. 1.13 The pressure dependence of **a** the nearest-neighbour Ge–O, O–O and Ge–Ge distances and **b** the Ge–O and O–O coordination numbers. The results from NDIS experiments (■) and molecular dynamics simulations using the DIPPIM (broken (red) curves) [109] are compared to those obtained from the neutron diffraction work of Drewitt et al. [110] [(green) ●] and Salmon et al. [111] [(blue) ▲]. In (b) the Ge–O coordination numbers from IXS experiments [116] are also shown [(red) ◇]. The figure is taken from Wezka et al. [109]. © IOP Publishing. Reproduced by permission of IOP Publishing. All rights reserved

The DIPPIM molecular dynamics results are in good accord with the measured pressure dependence of the difference functions in both reciprocal and real space (Figs. 1.11 and 1.12), an agreement that also extends to the mean nearest-neighbour distances, coordination numbers, and O–Ge–O and Ge–O–Ge bond angles (Figs. 1.13 and 1.14). The model’s predictions for the reduced density dependence of the fractions of four-, five- and six-fold coordinated Ge atoms, and of twofold and threefold coordinated oxygen atoms, are shown in Fig. 1.14. This dependence for the fractions of GeO_4 , GeO_5 and GeO_6 units is not in agreement with estimates based on inelastic x-ray scattering (IXS) experiments [116], a discrepancy that may originate from the use of data from crystalline standards containing trigonal bipyramidal GeO_5 units to analyse the measured IXS spectra: the predominant GeO_5 units found from the molecular dynamics results are distorted square pyramids.¹¹ In contrast, other

¹¹ As shown in Fig. 1.13b, the Ge–O coordination number obtained at ~ 8 GPa ($\rho/\rho_0 \sim 1.4$) from the IXS experiments is large relative to the value obtained from neutron diffraction experiments in a regime for which the IXS data give, relative to molecular dynamics, a much greater fraction of GeO_6 units relative to GeO_4 and GeO_5 units (Fig. 1.14a).

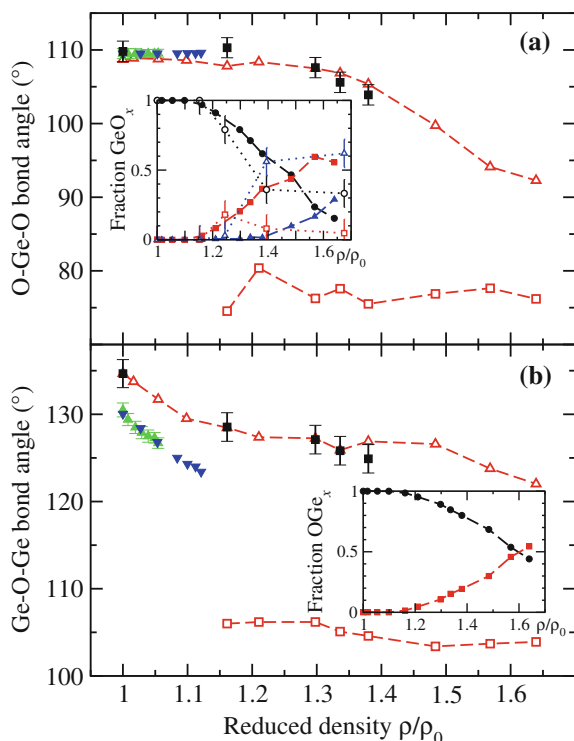


Fig. 1.14 The reduced density ρ/ρ_0 dependence of the **a** O–Ge–O and **b** Ge–O–Ge bond angles as measured for GeO₂ glass [109] (■) and for the α -quartz polymorph of crystalline GeO₂ in the work of Jorgensen [112] [(green) ▲] and Glinnemann et al. [113] [(blue) ▼]. Also shown are the peak positions in the DIPPIM bond angle distributions for the glass, where the appearance of a second branch at higher reduced densities corresponds to the development of an additional peak or shoulder in these bond-angle distributions. The first branch originates at ambient density from tetrahedral GeO₄ motifs [(red) △], and the second branch appears at higher densities as these motifs are replaced by GeO₅ and GeO₆ units [(red) □]. The insets show the DIPPIM results for the density dependence of (a) the fraction of GeO_x species, where $x = 4$ (●), 5 [(red) ■] or 6 [(blue) ▲], and (b) the fraction of OGe_x species, where $x = 2$ (●) or 3 [(red) ■]. In (a), the inset also shows the fraction of GeO_x species from IXS experiments [116] where $x = 4$ (○), 5 [(red) □] or 6 [(blue) △]. The figure is taken from Wezka et al. [109]. © IOP Publishing. Reproduced by permission of IOP Publishing. All rights reserved

models for the pressure-induced structural changes in GeO₂ glass, as obtained by using the Oeffner-Elliott two-body potentials [117] in classical molecular dynamics simulations [118–122] or first-principles molecular dynamics simulations using a generalised gradient approximation [123], do not reproduce basic features such as the pressure dependence of the measured Ge–O bond lengths and coordination numbers (Fig. 1.15). The Oeffner-Elliott potentials were initially employed to model the α -quartz and rutile-like phases of GeO₂ and the phase transition between the α - and β -quartz phases of this material [117].

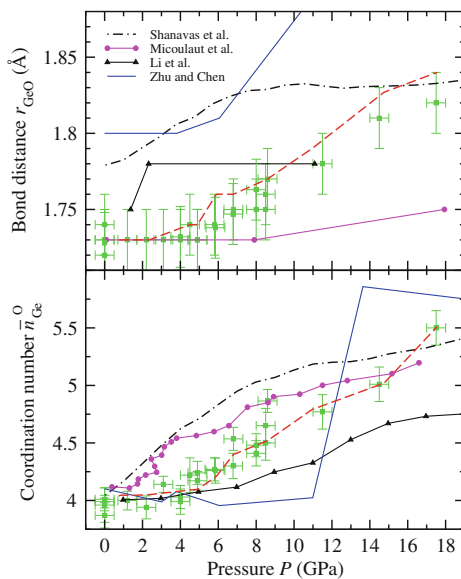


Fig. 1.15 The pressure dependence of the Ge–O bond distance r_{GeO} and coordination number $\bar{n}_{\text{Ge}}^{\text{O}}$ for GeO_2 glass. The results from neutron diffraction are shown by the (green) squares with error bars [109–111] and the results from different molecular dynamics simulations are given by the curves. The results from the DIPPIM interaction potentials [broken light (red) curves] are in agreement with the experimental data. In contrast, the results of Micoulaut et al. [118, 119] [solid (magenta) curves with circles], Shanavas et al. [120] [chained dark (black) curves] and Li et al. [122] [solid curves with triangles] obtained by using the Oeffner-Elliott interaction potentials [117], and the results of Zhu and Chen [123] [solid dark (blue) curves] obtained by using first-principles methods, are not consistent with the measured data. The figure is adapted from Wezka et al. [109]

1.6 Conclusions and Future Perspectives

This chapter has focussed on several prototypical MX_2 network glass-forming materials in order to illustrate the benefits of having detailed structural information from experiment to guide in the development of realistic molecular dynamics models. Many of the pertinent experimental results have originated from the NDIS method because this can be used to provide information at the partial structure factor level.

In the case of ZnCl_2 it was found that the main structural features can be accounted for within the framework of an ionic interaction model, provided that anion polarisation effects are taken into account. This led to a systematic investigation of the relationship between the structure and fragility of tetrahedral glass forming liquids where the anion polarisability was used as an adjustable parameter in order to change the network connectivity. The model reproduces the measured trends, and correlates increased fragility with an increase in number of edge-sharing units, thus emphasising the importance of these configurations on the dynamics of tetrahedral glass-forming liquids. In the case of GeSe_2 an ionic interaction model does not reproduce mea-

sured features such as homopolar bonds, and first-principles molecular dynamics need to be employed. The progression to the use in self-consistent calculations of the Becke-Lee-Yang-Parr (BLYP) functional has led to models that are in better agreement with the NDIS and other experimental results. Finally, in the case of GeO_2 under cold-compression, the parameterisation of a polarisable ion model using ab initio results has led to predictions for the pressure-induced structural changes that are in accord with experiment, and to insight into the mechanisms of density-driven network collapse.

When assessing the results obtained from a molecular dynamics model, it is valuable to make comparisons with diffraction data in both real and reciprocal space. For example, the short-range order will manifest itself by the appearance of a peak in a partial pair-distribution function at a small r -value, whereas the intermediate range order leads to a more subtle r -space modulation that will manifest itself by the appearance of an FSDP in the corresponding reciprocal space function e.g. $S_{\text{MM}}(k)$ [57]. It is therefore convenient to examine details of the short-range order of a model in real space, and details of the intermediate-range order of this model in reciprocal space. It can also be valuable to make a like-for-like comparison of a modelled r -space function with experiment by following the experimental procedure i.e. by taking a simulated reciprocal space function, truncating it at the value for k_{max} set by a diffractometer, and Fourier transforming (Sect. 1.2). Interestingly, although the quench rates used in simulation are fast, the simulated pair-correlation functions can be in good accord with experiment i.e. modelled glass structures are not necessarily those of the corresponding high-temperature liquids caught in time.

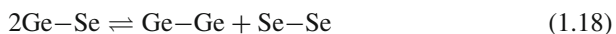
Once the correct theoretical scheme has been established, molecular dynamics models can be used to enrich the information about a material that can be extracted, and they can also be used to predict the changes in material properties that occur when e.g. new chemical species are added or the state conditions are varied. Indeed, one of the ultimate aims of making realistic atomistic models for network glass-forming systems is the development of new materials following the principles of rational design [124–126] i.e. the strategy of creating new glasses with the desired functionality, based on an ability to predict the structure of a glass and how this will affect its physical properties. The rational design approach stands to gain more ground as network glass-forming materials continue to reveal more and more of their structural secrets.

Acknowledgments It is a pleasure to thank everyone who has contributed towards the experimental programme of research at Bath and UEA into the nature of network glass-forming materials, including Ian Penfold, Chris Benmore, Paul Lond, Erol Okan, Jian Liu, Shuqin Xin, Jonathan Wasse, Takeshi Usuki, Ingrid Petri, Richard Martin, James Drewitt, Prae Chirawatkul, Dean Whittaker, Kamil Wezka, Keiron Pizzey, Ruth Rowlands, Annalisa Polidori and Harry Bone. Special thanks also go to Adrian Barnes (Bristol), Pierre Chieux (ILL), Wilson Crichton (ESRF), Gabriel Cuello (ILL), Henry Fischer (ILL) and Stefan Klotz (Paris) for their contributions to the experimental work; and to Mauro Boero (Strasbourg), Assil Bouzid (Strasbourg), Sébastien Le Roux (Strasbourg), Dario Marrocchelli (MIT), Carlo Massobrio (Strasbourg), Matthieu Micoulaut (Paris), Alfredo Pasquarello (Lausanne) and Mark Wilson (Oxford) for all their contributions on the molecular dynamics front. The latter are also thanked for agreeing to a close dialogue with the experimental teams, where the feedback has been mutually beneficial in helping to decode the complexity of

network glass-forming materials, and has also led to a fuller appreciation of both the advantages and limitations of experimental versus molecular dynamics methods. The support of the EPSRC (Grant: EP/J009741/1) and Institut Laue-Langevin (ILL) is gratefully acknowledged.

Appendix: Concentration of Defects in GeSe₂ Glass from the Law of Mass Action

Following Feltz [127, 128], consider the reversible reaction



where homopolar or defect bonds are formed in pairs, and for which the law of mass action gives an equilibrium constant

$$K = \frac{[\text{Ge-Ge}][\text{Se-Se}]}{[\text{Ge-Se}]^2} = \exp\left(-\frac{\Delta G}{RT}\right) \quad (1.19)$$

where $[\text{A-B}]$ represents the concentration of A-B bonds, ΔG is the standard reaction Gibbs energy, R is the molar gas constant, and T is the absolute temperature. From (1.18) it follows that the concentration of Ge-Ge or Se-Se defect bonds $n_d = [\text{Ge-Ge}] = [\text{Se-Se}]$ where the Ge-Ge homopolar bonds might be in ethane-like $\text{Se}_{3/2}\text{Ge-GeSe}_{3/2}$ units as suggested by ^{119}Sn Mössbauer spectroscopy experiments [83, 129] and the Se-Se homopolar bonds might be in dimers linking Ge-centred tetrahedra. Equation (1.19) can therefore be re-written as

$$\frac{n_d}{n_0} = \exp\left(-\frac{\Delta G}{2RT}\right) \quad (1.20)$$

where $n_0 \equiv [\text{Ge-Se}]$. If the concentration of defects is small such that $n_d \ll n_0$ then the latter is approximately equal to the concentration of Ge-Se bonds in a non-defected system.

ΔG can be estimated from the difference between the Ge-Se, Ge-Ge and Se-Se bond enthalpies which take values of 225, 188 and 227 kJ mol⁻¹, respectively, at 298 K i.e. $\Delta G \simeq \Delta H = 2 \times 225 - 188 - 227 = 35$ kJ mol⁻¹ [127]. Hence, an estimate for the fraction of defects in the melt at the glass transition temperature ($T_g = 665$ K) is given by $n_d/n_0 \simeq 0.042$. Alternatively, if $n_d \equiv N_d/V$ and $n_0 \equiv N_{\text{bond}}/V$, where N_d is the number of Ge-Ge or Se-Se homopolar bonds and N_{bond} is the total number of bonds, it follows that $N_d/N_{\text{bond}} \simeq 0.042$. This ratio is probably a lower limit because the value of ΔG used in the calculation is likely to decrease when the entropy term ΔS is taken into account ($\Delta G = \Delta H - T\Delta S$ if the absolute temperature T is constant), and the reaction enthalpy ΔH is likely to be smaller at T_g as compared to room temperature [127, 128].

Let the total number of atoms in the system be denoted by $N = N_{\text{Ge}} + N_{\text{Se}}$ where N_{Ge} and N_{Se} are the numbers of Ge and Se atoms, respectively, such that the atomic fractions are given by $c_{\text{Ge}} = N_{\text{Ge}}/N$ and $c_{\text{Se}} = N_{\text{Se}}/N$. From the NDIS results on GeSe_2 glass [22, 23], the coordination number for Ge–Ge homopolar bonds $\bar{n}_{\text{Ge}}^{\text{Ge}} = 0.25(5)$. If these bonds form only in pairs then $\bar{n}_{\text{Ge}}^{\text{Ge}} = (N_{\text{Ge,homo}} \times 1) / N_{\text{Ge}}$ such that the number of Ge–Ge bonds is given by $N_{\text{Ge-Ge}} = (\bar{n}_{\text{Ge}}^{\text{Ge}} \times N_{\text{Ge}}) / 2$ where the factor of two avoids double counting and $N_{\text{Ge}} = N/3$. It follows that $N_{\text{Ge-Ge}} = 0.042(8)N$. Similarly, from the NDIS results the coordination number for Se–Se homopolar bonds $\bar{n}_{\text{Se}}^{\text{Se}} = 0.20(5)$. If these bonds form only in pairs then $\bar{n}_{\text{Se}}^{\text{Se}} = (N_{\text{Se,homo}} \times 1) / N_{\text{Se}}$ such that the number of Se–Se bonds is given by $N_{\text{Se-Se}} = (\bar{n}_{\text{Se}}^{\text{Se}} \times N_{\text{Se}}) / 2$ where the factor of two avoids double counting and $N_{\text{Se}} = 2N/3$. It follows that $N_{\text{Se-Se}} = 0.067(17)N$. Thus, within the experimental error, $N_{\text{Ge-Ge}} \sim N_{\text{Se-Se}}$ as in the model of Feltz [127] such that $N_d \simeq (N_{\text{Ge-Ge}} + N_{\text{Se-Se}}) / 2 = 0.05(2)N$.

For GeSe_2 , the number of Ge–Se bonds in a non-defected system $N_{\text{bond}} = (N_{\text{Ge}}Z_{\text{Ge}} + N_{\text{Se}}Z_{\text{Se}})/2 = (c_{\text{Ge}}Z_{\text{Ge}} + c_{\text{Se}}Z_{\text{Se}})N/2$ where Z_{α} is the number of bonds formed by chemical species α . Since $Z_{\text{Ge}} = 4$, $Z_{\text{Se}} = 2$, $c_{\text{Ge}} = 1/3$, $c_{\text{Se}} = 2/3$ it follows that $N_{\text{bond}} = 4N/3$. Thus $N_d/N_{\text{bond}} \simeq 0.04(2)$ for the NDIS results, which is in agreement with the value $N_d/N_{\text{bond}} \simeq 0.042$ estimated by using the law of mass action.

References

1. M. Yamane, Y. Asahara, *Glasses for Photonics* (Cambridge University Press, Cambridge, 2000)
2. S.Y. Park, S.K. Lee, *Geochim. Cosmochim. Acta* **80**, 125 (2012)
3. R.L. McGreevy, L. Pusztai, *Mol. Simul.* **1**, 359 (1988)
4. R.L. McGreevy, *J. Phys.: Condens. Matter* **13**, R877 (2001)
5. A.K. Soper, *Chem. Phys.* **202**, 295 (1996)
6. A.K. Soper, *Phys. Rev. B* **72**, 104204 (2005)
7. D.A. Keen, *Phase Transitions* **61**, 109 (1997)
8. M.G. Tucker, D.A. Keen, M.T. Dove, K. Trachenko, *J. Phys.: Condens. Matter* **17**, S67 (2005)
9. A.K. Soper, *J. Phys.: Condens. Matter* **19**, 335206 (2007)
10. A.K. Soper, C.J. Benmore, *Phys. Rev. Lett.* **108**, 259603 (2012)
11. A. Zeidler, P.S. Salmon, H.E. Fischer, J.C. Neuefeind, J.M. Simonson, H. Lemmel, H. Rauch, T.E. Markland, *Phys. Rev. Lett.* **108**, 259604 (2012)
12. L.B. Skinner, A.C. Barnes, P.S. Salmon, H.E. Fischer, J.W.E. Drewitt, V. Honkimäki, *Phys. Rev. B* **85**, 064201 (2012)
13. L.B. Skinner, A.C. Barnes, P.S. Salmon, L. Hennem, H.E. Fischer, C.J. Benmore, S. Kohara, J.K.R. Weber, A. Bytchkov, M.C. Wilding, J.B. Parise, T.O. Farmer, I. Pozdnyakova, S.K. Tumber, K. Ohara, *Phys. Rev. B* **87**, 024201 (2013)
14. S. Biggin, J.E. Enderby, *J. Phys. C: Solid State Phys.* **14**, 3129 (1981)
15. P.S. Salmon, R.A. Martin, P.E. Mason, G.J. Cuello, *Nature* **435**, 75 (2005)
16. A. Zeidler, P.S. Salmon, R.A. Martin, T. Usuki, P.E. Mason, G.J. Cuello, S. Kohara, H.E. Fischer, *Phys. Rev. B* **82**, 104208 (2010)
17. A. Zeidler, P. Chirawatkul, P.S. Salmon, T. Usuki, S. Kohara, H.E. Fischer, W.S. Howells, *J. Non-Cryst. Solids* **407**, 235 (2015)

18. M. Wilson, P.A. Madden, J. Phys.: Condens. Matter **5**, 6833 (1993)
19. P.A. Madden, M. Wilson, Chem. Soc. Rev. **25**, 339 (1996)
20. M. Wilson, Phys. Chem. Chem. Phys. **14**, 12701 (2012)
21. I.T. Penfold, P.S. Salmon, Phys. Rev. Lett. **67**, 97 (1991)
22. I. Petri, P.S. Salmon, H.E. Fischer, Phys. Rev. Lett. **84**, 2413 (2000)
23. P.S. Salmon, I. Petri, J. Phys.: Condens. Matter **15**, S1509 (2003)
24. M. Cobb, D.A. Drabold, R.L. Cappelletti, Phys. Rev. B **54**, 12162 (1996)
25. M. Cobb, D.A. Drabold, Phys. Rev. B **56**, 3054 (1997)
26. C. Massobrio, A. Pasquarello, R. Car, Phys. Rev. Lett. **80**, 2342 (1998)
27. C. Massobrio, A. Pasquarello, R. Car, J. Am. Chem. Soc. **121**, 2943 (1999)
28. C. Massobrio, A. Pasquarello, R. Car, Comput. Mater. Sci. **17**, 115 (2000)
29. X. Zhang, D.A. Drabold, Phys. Rev. B **62**, 15695 (2000)
30. C. Massobrio, A. Pasquarello, R. Car, Phys. Rev. B **64**, 144205 (2001)
31. C. Massobrio, M. Celino, A. Pasquarello, Phys. Rev. B **70**, 174202 (2004)
32. C. Massobrio, A. Pasquarello, J. Phys.: Condens. Matter **19**, 415111 (2007)
33. C. Massobrio, A. Pasquarello, Phys. Rev. B **75**, 014206 (2007)
34. C. Massobrio, A. Pasquarello, Phys. Rev. B **77**, 144207 (2008)
35. M. Wilson, B.K. Sharma, C. Massobrio, J. Chem. Phys. **128**, 244505 (2008)
36. M. Micoulaut, R. Vuilleumier, C. Massobrio, Phys. Rev. B **79**, 214205 (2009)
37. C. Massobrio, Lect. Notes Phys. **795**, 343 (2010)
38. C. Massobrio, M. Micoulaut, P.S. Salmon, Solid State Sci. **12**, 199 (2010)
39. M. Micoulaut, S. Le Roux, C. Massobrio, J. Chem. Phys. **136**, 224504 (2012)
40. A. Bouzid, C. Massobrio, J. Chem. Phys. **137**, 046101 (2012)
41. Y. Liang, C.R. Miranda, S. Scandolo, High Press. Res. **28**, 35 (2008)
42. C. Massobrio, M. Celino, P.S. Salmon, R.A. Martin, M. Micoulaut, A. Pasquarello, Phys. Rev. B **79**, 174201 (2009)
43. D. Marrocchelli, M. Salanne, P.A. Madden, J. Phys.: Condens. Matter **22**, 152102 (2010)
44. H.E. Fischer, A.C. Barnes, P.S. Salmon, Rep. Prog. Phys. **69**, 233 (2006)
45. T.E. Faber, J.M. Ziman, Philos. Mag. **11**, 153 (1965)
46. J.E. Enderby, D.M. North, P.A. Egelstaff, Philos. Mag. **14**, 961 (1966)
47. P.S. Salmon, A. Zeidler, Phys. Chem. Chem. Phys. **15**, 15286 (2013)
48. A.B. Bhatia, D.E. Thornton, Phys. Rev. B **2**, 3004 (1970)
49. E. Lorch, J. Phys. C: Solid State Phys. **2**, 229 (1969)
50. P.S. Salmon, J. Phys.: Condens. Matter **18**, 11443 (2006)
51. F.G. Edwards, R.A. Howe, J.E. Enderby, D.I. Page, J. Phys. C: Solid State Phys. **11**, 1053 (1978)
52. R.L. McGreevy, E.W.J. Mitchell, J. Phys. C: Solid State Phys. **15**, 5537 (1982)
53. S. Biggin, J.E. Enderby, J. Phys. C: Solid State Phys. **14**, 3577 (1981)
54. S. Biggin, M. Gay, J.E. Enderby, J. Phys. C: Solid State Phys. **17**, 977 (1984)
55. R.J. Newport, R.A. Howe, N.D. Wood, J. Phys. C: Solid State Phys. **18**, 5249 (1985)
56. R.D. Shannon, Acta Crystallogr. A **32**, 751 (1976)
57. P.S. Salmon, Proc. R. Soc. Lond. A **445**, 351 (1994)
58. P.S. Salmon, Proc. R. Soc. Lond. A **437**, 591 (1992)
59. P.S. Salmon, J. Phys.: Condens. Matter **19**, 455208 (2007)
60. J.E. Enderby, A.C. Barnes, Rep. Prog. Phys. **53**, 85 (1990)
61. M. Wilson, P.S. Salmon, Phys. Rev. Lett. **103**, 157801 (2009)
62. M. Wilson, P.A. Madden, Phys. Rev. Lett. **80**, 532 (1998)
63. B.K. Sharma, M. Wilson, J. Phys.: Condens. Matter **20**, 244123 (2008)
64. P.S. Salmon, J. Phys.: Condens. Matter **17**, S3537 (2005)
65. P.S. Salmon, A.C. Barnes, R.A. Martin, G.J. Cuello, Phys. Rev. Lett. **96**, 235502 (2006)
66. M.J.L. Sangster, M. Dixon, Adv. Phys. **25**, 247 (1976)
67. N.C. Pyper, in *Advances in Solid State Chemistry*, vol. 2, ed. by C.R.A. Catlow (JAI Press, London, 1991), p. 223
68. R. Kjellander, B. Forsberg, J. Phys. A: Math. Gen. **38**, 5405 (2005)

69. R. Evans, R.J.F. Leote de Carvalho, J.R. Henderson, D.C. Hoyle, *J. Chem. Phys.* **100**, 591 (1994)
70. R.J.F. Leote de Carvalho, R. Evans, *Mol. Phys.* **83**, 619 (1994)
71. C. Grodon, M. Dijkstra, R. Evans, R. Roth, *J. Chem. Phys.* **121**, 7869 (2004)
72. C.A. Angell, *Science* **267**, 1924 (1995)
73. V.N. Novikov, Y. Ding, A.P. Sokolov, *Phys. Rev. E* **71**, 061501 (2005)
74. J. Málek, J. Šhánělová, *J. Non-Cryst. Solids* **243**, 116 (1999)
75. E.A. Pavlatou, S.N. Yannopoulos, G.N. Papatheodorou, G. Fytas, *J. Phys. Chem. B* **101**, 8748 (1997)
76. J. Ruska, H. Thurn, *J. Non-Cryst. Solids* **22**, 277 (1976)
77. J.A.E. Desa, A.C. Wright, J. Wong, R.N. Sinclair, *J. Non-Cryst. Solids* **51**, 57 (1982)
78. J. Neuefeind, K.-D. Liss, *Ber. Bunsenges. Phys. Chem.* **100**, 1341 (1996)
79. A. Zeidler, J.W.E. Drewitt, P.S. Salmon, A.C. Barnes, W.A. Crichton, S. Klotz, H.E. Fischer, C.J. Benmore, S. Ramos, A.C. Hannon, *J. Phys.: Condens. Matter* **21**, 474217 (2009)
80. P.S. Salmon, *J. Non-Cryst. Solids* **353**, 2959 (2007)
81. G. Dittmar, H. Schäfer, *Acta Crystallogr. B* **32**, 2726 (1976)
82. S.B. Mamedov, N.D. Aksenov, L.L. Makarov, Yu.F. Batrakov, *J. Non-Cryst. Solids* **195**, 272 (1996)
83. P. Boolchand, W.J. Bresser, *Philos. Mag. B* **80**, 1757 (2000)
84. J.P. Perdew, Y. Wang, *Phys. Rev. B* **45**, 13244 (1992)
85. A.D. Becke, *Phys. Rev. A* **38**, 3098 (1988)
86. C. Lee, W. Yang, R.G. Parr, *Phys. Rev. B* **37**, 785 (1988)
87. K. Wezka, A. Bouzid, K.J. Pizze, P.S. Salmon, A. Zeidler, S. Klotz, H.E. Fischer, C.L. Bull, M.G. Tucker, M. Boero, S. Le Roux, C. Tugène, C. Massobrio, *Phys. Rev. B* **90**, 054206 (2014)
88. L. Giacomazzi, C. Massobrio, A. Pasquarello, *Phys. Rev. B* **75**, 174207 (2007)
89. L. Giacomazzi, C. Massobrio, A. Pasquarello, *J. Phys.: Condens. Matter* **23**, 295401 (2011)
90. P. Vashishta, R.K. Kalia, G.A. Antonio, I. Ebbsjö, *Phys. Rev. Lett.* **62**, 1651 (1989)
91. P. Vashishta, R.K. Kalia, I. Ebbsjö, *Phys. Rev. B* **39**, 6034 (1989)
92. H. Iyetomi, P. Vashishta, R.K. Kalia, *Phys. Rev. B* **43**, 1726 (1991)
93. P. Vashishta, R.K. Kalia, J.P. Rino, I. Ebbsjö, *Phys. Rev. B* **41**, 12197 (1990)
94. B.K. Sharma, M. Wilson, *Phys. Rev. B* **73**, 060201(R) (2006)
95. S.N. Yannopoulos, A.G. Kalampounias, A. Chrissanthopoulos, G.N. Papatheodorou, *J. Chem. Phys.* **118**, 3197 (2003)
96. M. Celino, C. Massobrio, *Phys. Rev. Lett.* **90**, 125502 (2003)
97. Q. Mei, C.J. Benmore, S. Sen, R. Sharma, J.L. Yarger, *Phys. Rev. B* **78**, 144204 (2008)
98. G.N. Greaves, S. Sen, *Adv. Phys.* **56**, 1 (2007)
99. P.S. Salmon, A.C. Barnes, R.A. Martin, G.J. Cuello, *J. Phys.: Condens. Matter* **19**, 415110 (2007)
100. L. Giacomazzi, P. Umari, A. Pasquarello, *Phys. Rev. B* **74**, 155208 (2006)
101. M. Wilson, B.K. Sharma, *J. Chem. Phys.* **128**, 214507 (2008)
102. V.V. Brazhkin, A.G. Lyapin, *J. Phys.: Condens. Matter* **15**, 6059 (2003)
103. M.C. Wilding, M. Wilson, P.F. McMillan, *Chem. Soc. Rev.* **35**, 964 (2006)
104. G.N. Greaves, M.C. Wilding, S. Fearn, D. Langstaff, F. Kargl, S. Cox, Q. Vu Van, O. Majerus, C.J. Benmore, R. Weber, C.M. Martin, L. Hennen, *Science* **322**, 566 (2008)
105. A.C. Barnes, L.B. Skinner, P.S. Salmon, A. Bytchkov, I. Pozdnyakova, T.O. Farmer, H.E. Fischer, *Phys. Rev. Lett.* **103**, 225702 (2009)
106. A.C. Barnes, L.B. Skinner, P.S. Salmon, A. Bytchkov, I. Pozdnyakova, T.O. Farmer, H.E. Fischer, *Phys. Rev. Lett.* **106**, 119602 (2011)
107. D. Daisenberger, T. Deschamps, B. Champagnon, M. Mezouar, R.Q. Cabrera, M. Wilson, P.F. McMillan, *J. Phys. Chem. B* **115**, 14246 (2011)
108. C.S. Mariani, L.W. Hobbs, *J. Non-Cryst. Solids* **124**, 242 (1990)
109. K. Wezka, P.S. Salmon, A. Zeidler, D.A.J. Whittaker, J.W.E. Drewitt, S. Klotz, H.E. Fischer, D. Marrocchelli, *J. Phys.: Condens. Matter* **24**, 502101 (2012)

- 110. J.W.E. Drewitt, P.S. Salmon, A.C. Barnes, S. Klotz, H.E. Fischer, W.A. Crichton, *Phys. Rev. B* **81**, 014202 (2010)
- 111. P.S. Salmon, J.W.E. Drewitt, D.A.J. Whittaker, A. Zeidler, K. Wezka, C.L. Bull, M.G. Tucker, M.C. Wilding, M. Guthrie, D. Marrocchelli, *J. Phys.: Condens. Matter* **24**, 415102 (2012)
- 112. J.D. Jorgensen, *J. Appl. Phys.* **49**, 5473 (1978)
- 113. J. Glinnemann, H.E. King Jr, H. Schulz, Th. Hahn, S.J. La Placa, F. Dacol, *Z. Kristallogr.* **198**, 177 (1992)
- 114. X. Hong, G. Shen, V.B. Prakapenka, M. Newville, M.L. Rivers, S.R. Sutton, *Phys. Rev. B* **75**, 104201 (2007)
- 115. D. Marrocchelli, M. Salanne, P.A. Madden, C. Simon, P. Turq, *Mol. Phys.* **107**, 443 (2009)
- 116. G. Lelong, L. Cormier, G. Ferlat, V. Giordano, G.S. Henderson, A. Shukla, G. Calas, *Phys. Rev. B* **85**, 134202 (2012)
- 117. R.D. Oeffner, S.R. Elliott, *Phys. Rev. B* **58**, 14791 (1998)
- 118. M. Micoulaut, *J. Phys.: Condens. Matter* **16**, L131 (2004)
- 119. M. Micoulaut, Y. Guissani, B. Guillot, *Phys. Rev. E* **73**, 031504 (2006)
- 120. K.V. Shanavas, N. Garg, S.M. Sharma, *Phys. Rev. B* **73**, 094120 (2006)
- 121. M. Micoulaut, X. Yuan, L.W. Hobbs, *J. Non-Cryst. Solids* **353**, 1961 (2007)
- 122. T. Li, S. Huang, J. Zhu, *Chem. Phys. Lett.* **471**, 253 (2009)
- 123. X.F. Zhu, L.F. Chen, *Phys. B* **404**, 4178 (2009)
- 124. J.D. Martin, S.J. Goettler, N. Fossé, L. Iton, *Nature* **419**, 381 (2002)
- 125. P.S. Salmon, *Nat. Mater.* **1**, 87 (2002)
- 126. M.M. Smedskjaer, J.C. Mauro, S. Sen, Y. Yue, *Chem. Mater.* **22**, 5358 (2010)
- 127. A. Feltz, in *Physics of Disordered Materials*, ed. by D. Adler, H. Fritzche, S.R. Ovshinsky (Plenum, New York, 1985), p. 203
- 128. A. Feltz, *Amorphous Inorganic Materials and Glasses* (VCH, Weinheim, 1993), p. 97
- 129. P. Boolchand, J. Grothaus, W.J. Bresser, P. Suranyi, *Phys. Rev. B* **25**, 2975 (1982)

Molecular Dynamics Simulations of Disordered Materials
From Network Glasses to Phase-Change Memory Alloys

Massobrio, C.; Du, J.; Bernasconi, M.; Salmon, P.S.

(Eds.)

2015, XIX, 529 p. 263 illus., 212 illus. in color.,

Hardcover

ISBN: 978-3-319-15674-3